Virulence

ISSN: 2150-5594 (Print) 2150-5608 (Online) Journal homepage: www.tandfonline.com/journals/kvir20

Inhibitors of GapN-dependent NADPH supply as potential lead compounds for novel therapeutics against *Streptococcus pyogenes*

Isabell Schütt, Philip Einwohlt , Anna-Maria Wandinger , Jonathan Teuffel , Regina Wirsing , Ben H. Hlawatschke , Hanna L. Fehlauer , Sebastian Bothe , Nicole Bader , Emanuele Monaci , Bernd Kreikemeyer, Hermann Schindelin , Rebecca C. Wade & Tomas Fiedler

To cite this article: Isabell Schütt, Philip Einwohlt , Anna-Maria Wandinger , Jonathan Teuffel , Regina Wirsing , Ben H. Hlawatschke , Hanna L. Fehlauer , Sebastian Bothe , Nicole Bader , Emanuele Monaci , Bernd Kreikemeyer, Hermann Schindelin , Rebecca C. Wade & Tomas Fiedler (2026) Inhibitors of GapN-dependent NADPH supply as potential lead compounds for novel therapeutics against *Streptococcus pyogenes*, Virulence, 17:1, 2609393, DOI: 10.1080/21505594.2025.2609393

To link to this article: https://doi.org/10.1080/21505594.2025.2609393

VIRULENCE
2026, VOL. 17, NO. 1, 2609393
https://doi.org/10.1080/21505594.2025.2609393

Taylor & Francis
Taylor & Francis Group

BACTERIAL PATHOGENESIS

OPEN ACCESS Check for updates

Inhibitors of GapN-dependent NADPH supply as potential lead compounds for novel therapeutics against *Streptococcus pyogenes*

Isabell Schütt [a], Philip Einwohlt[a*], Anna-Maria Wandinger[b**], Jonathan Teuffel[c,d,e], Regina Wirsing[b], Ben H. Hlawatschke[a], Hanna L. Fehlauer[a], Sebastian Bothe[b], Nicole Bader[b], Emanuele Monaci[c,f,#], Bernd Kreikemeyer [a], Hermann Schindelin[b], Rebecca C. Wade[c,d,f,g], and Tomas Fiedler [a]

[a]Institute of Medical Microbiology, Virology, and Hygiene, Rostock University Medical Center, Rostock, Germany; [b]Rudolf Virchow Center for Integrative and Translational Bioimaging, University of Würzburg, Würzburg, Germany; [c]Molecular and Cellular Modeling Group, Heidelberg Institute for Theoretical Studies, Heidelberg, Germany; [d]Faculty of Engineering Sciences, Heidelberg University, Heidelberg, Germany; [e]Graduate School of Mathematical and Computational Methods for the Sciences (HGS mathcomp), Heidelberg University, Heidelberg, Germany; [f]Center for Molecular Biology (ZMBH), DKFZ-ZMBH Alliance, Heidelberg University, Heidelberg, Germany; [g]Interdisciplinary Center for Scientific Computing (IWR), Heidelberg University, Heidelberg, Germany

ABSTRACT

Infections with *Streptococcus pyogenes* are among the most important diseases caused by bacteria and are responsible for around 500,000 deaths every year. In 2024, macrolide-resistant *S. pyogenes* was added to the WHO's list of priority pathogens. The non-phosphorylating glyceraldehyde-3-phosphate dehydrogenase GapN has been identified as a potential drug target in *S. pyogenes*. SpyGapN is the major NADP-reducing enzyme in these bacteria as they lack the oxidative part of the pentose phosphate pathway. In this study, *in silico* docking of compound libraries to the glyceraldehyde 3-phosphate binding pocket of SpyGapN was used to screen for potential competitive inhibitors. Among the candidates identified with this approach, 1,2-dihydroxyethane-1,2-disulfonate (glyoxal bisulfite) showed the strongest inhibition of SpyGapN activity *in vitro*. In a complementary approach, crystallographic fragment screening was conducted, which identified the ultra-low-molecular-weight compounds pyrimidine-5-amine and 4-hydroxypyridazine targeting the cofactor-binding pocket of SpyGapN. Both low-molecular-weight compounds were experimentally confirmed to inhibit the activity of purified SpyGapN. Combinations of glyoxal bisulfite with either pyrimidine-5-amine or 4-hydroxypyridazine enhanced the inhibitory effect of SpyGapN. Glyoxal bisulfite was able to kill *S. pyogenes*. This effect was accelerated by combining glyoxal bisulfite with 4-hydroxypyridazine. While these findings suggest that inhibition of SpyGapN probably contributes to the observed antibacterial activity, the exact mechanism of action remains to be confirmed, as the compounds also affect other G3P-converting enzymes. Nevertheless, these compounds provide a promising starting point for the development of more specific SpyGapN inhibitors.

ARTICLE HISTORY
Received 18 July 2025
Revised 3 December 2025
Accepted 21 December 2025

KEYWORDS
Streptococcus pyogenes; GapN; drug target; computational docking; antimicrobials; glyoxal bisulfite

Introduction

Streptococcus pyogenes, also referred to as group A streptococcus (GAS), annually causes more than 600 million infections worldwide, resulting in an estimated half a million deaths each year [1]. The majority of these cases are self-limiting purulent infections of the skin or the mucosa of the upper respiratory tract. Severe cases include streptococcal toxic shock syndrome and necrotizing fasciitis or post-infection sequelae such as acute glomerulonephritis or rheumatic heart disease (RHD), which is estimated to develop in about 60% of patients subsequent to repeated acute rheumatic fever. It has been reported that, without secondary prophylaxis or modern medical care, approximately 1.5% of patients with RHD die annually, making it the most common fatal sequela [1]. More recent studies report that globally, RHD itself accounts for 1.6% of all cardiovascular disease-related deaths, resulting in approximately 300,000 deaths annually [2,3].

Despite this, most *S. pyogenes* infections are treated outside the hospital, with penicillin as the first-line antibiotic. Alternatively, macrolide antibiotics are frequently prescribed. While *S. pyogenes* is generally susceptible to penicillin, strains with reduced penicillin susceptibility caused by specific mutations in the penicillin-binding protein PBP2x have been repeatedly isolated from patients recently [4–6]. Several nonsynonymous *pbp2x*

CONTACT Tomas Fiedler tomas.fiedler@med.uni-rostock.de
*Present address: Institute for Systemic Inflammation Research, University of Lübeck, Lübeck, Germany.
**Present address: Department of Photobiotechnology, Ruhr University Bochum, Bochum, Germany.
#Present address: Lead Discovery Center GmbH, Planegg, Germany.
Supplemental data for this article can be accessed online at https://doi.org/10.1080/21505594.2025.2609393

substitutions have been identified globally in about 2% of more than 7000 analyzed *S. pyogenes* isolates [4], including T553K in the United States [6], M593T and P601L in Iceland [5], and further unspecified substitutions reported from Japan [7]. These strains may have the potential to develop full penicillin resistance [5]. Macrolide resistance frequently occurs in *S. pyogenes* and is a matter of increasing concern, especially in invasive infections [8,9]. Consequently, macrolide-resistant GAS have recently been added to the WHO Bacterial Priority Pathogens List [10].

Various approaches have been pursued to combat *S. pyogenes* infections using means other than traditional antibiotics. A crucial objective is and has been the development of effective vaccines against *S. pyogenes* [11,12]. Especially the highly abundant surface-associated M protein has been tested as a target, with vaccines covering up to 30 serologically distinguishable variants of the protein [13,14]. Most recently, efforts were made to develop mRNA-based vaccines covering multiple conserved surface antigens [15]. Although promising results have been obtained with both protein and mRNA-based approaches, no *S. pyogenes* vaccine has been approved for standard use in humans to date [12]. The serological heterogeneity of *S. pyogenes*, with about 270 different sequence versions of the M protein gene [16], dozens of different pilus types [17,18], and a variable array of other surface-associated structures in combination with the risk of autoimmune reactions, renders the development of an efficient vaccine a major challenge.

In addition to vaccine development, several potential new antimicrobial agents have been investigated that target either key virulence or fitness factors of *S. pyogenes* [19–22] or biological processes essential for the survival of the bacteria [23,24]. These include antisense peptide nucleic acids [25,26] antimicrobial peptides [27–29], derivatives of existing drugs [24], and newly identified compounds [30]. None of those, however, has made it to clinical use yet.

In our approach, we aimed at discovering new antimicrobial compounds that specifically combat *S. pyogenes* without largely impacting other bacteria. We previously identified a glycolytic enzyme, the non-phosphorylating glyceraldehyde 3-phosphate (G3P) dehydrogenase GapN, as a promising target [31]. The enzyme catalyzes the irreversible oxidation of glyceraldehyde 3-phosphate to 3-phosphoglycerate coupled to the reduction of $NADP^+$ to NADPH, as a phosphate-independent alternative to the conventional glyceraldehyde 3-phosphate dehydrogenase (GAPDH). While the latter exclusively uses NAD^+ as a co-factor, GapN specifically uses $NADP^+$ [31]. This feature renders the enzyme the primary source of NADPH in *S. pyogenes*, as the bacteria lack the oxidative part of the pentose phosphate pathway (oxPPP) that provides NADPH in most bacteria [32]. In line with this, the *gapN* gene was identified as an essential part of the *S. pyogenes* core genome [33]. In previous work, we could show that antisense-based knockdown of *gapN* specifically kills *S. pyogenes* and other streptococci lacking the oxPPP, while streptococci carrying the oxPPP genes were not susceptible to the *gapN* knockdown [31]. We determined a high-resolution crystal structure of the apo GapN wild-type and active site C284S variant from *S. pyogenes* [PDB entries 7PKJ (wild-type at 2 Å resolution) and 7PKC (C284S at 1.5 Å resolution)] and compared the wild-type to a homology model of a complementary holo-structure including G3P and $NADP^+$. After validating this homology model's ability to serve in the identification of inhibitor candidates via docking of erythrose-4-phosphate (E4P) [31], we here used it as a basis for *in silico* docking analysis to identify potential specific inhibitors of GapN. The results were validated against a newly determined 1.4 Å resolution crystal structure of a ternary *S. pyogenes* GapN-$NADP^+$-G3P complex. Furthermore, a crystallographic fragment screening campaign identified four hits, which were located either in the substrate-binding site or in the region where the nicotinamide moiety of NADPH is located, and these were assessed by computational docking. By combining the results of these two approaches to enzyme inhibitor discovery, we identified compounds that synergistically kill *S. pyogenes in vitro*.

Materials and methods

Bacterial strains and culture conditions

S. pyogenes M49 strain 591 [34] was grown in Todd–Hewitt broth supplemented with 1% yeast extract (THY) medium at 37°C under a 5% CO_2-enriched atmosphere. Recombinant *Escherichia coli* BL21 (DE3) and DH5α strains carrying pASK-IBA6 or pASK-IBA7 derivatives were grown in Lysogeny Broth (LB) medium containing 100 mg/l ampicillin at 37°C under ambient air.

Homology modeling of S. pyogenes GapN

Homology modeling was performed following our workflow for modeling the holo-structure of GapN from *S. pyogenes* described previously [31]. Briefly, we utilized the SWISS-MODEL webserver [35] and the sequence from Eisenberg et al. [31]. The template was the holo-structure of GapN from *S. mutans* solved by Cobesi et al. (PBD-ID 1QI1) [36]. The $NADP^+$ and

G3P ligands were manually inserted by superposition onto the template structure in PyMol [37].

Molecular docking

Molecular docking of inhibitor candidates with GLIDE [38] was conducted with the same parameters and on the homology model-based receptor grid generated in [31]. All preparation, docking, and analysis steps were performed in the Maestro environment [39] (Schrödinger release: 2020r2, Schrödinger, LLC; New York, NY, US, 2020). The "PrepWizard" program was used to protonate the protein at pH 7.0 ± 4.0, assign bond orders, and perform a restrained energy minimization with the OPLS2005 force field. The receptor grid was centered on the inserted G3P substrate and vdW- and ligand scaling were set to 1.0 and 0.8 times, respectively. Inhibitor-candidate libraries, e.g. generated with the RealSpace navigator software were imported into Maestro as two-dimensional sdf, pdb, or mol2 files. The compounds were prepared with "LigPrep" to assign protonation states using Epik at pH 7.0 ± 3.0, and to assign OPLS2005 parameters. If no three-dimensional information was available, the "ignore chirality" option was selected to generate up to 32 possible stereoisomers per compound.

Standard precision docking was performed with default parameters set to yield three docking poses per ligand. The poses were assessed by docking scores and visual inspection, with interesting candidates being selected according to (1) a comparable or better docking score (defined as ≤ −7 kcal/mol) of the highest ranked pose than the native G3P substrate, (2) a reasonable docking pose without severe clashes and plausible molecular interactions, and (3) commercial availability of the compound in the identified stereoisomer or racemic mixture.

Assessment of the compounds by redocking them to the subsequently solved holo-structure of GapN from *S. pyogenes* was conducted identically but with a more recent version of Maestro (Schrödinger release 2022r4). This approach was validated by redocking G3P to the previously used homology model using the more recent Schrödinger release (2022r4), which resulted in a very similar binding pose (RMSD = 1.1 Å) and a docking score of −7.4 kcal/mol. The minor deviation of this value from the previously measured docking score of −7.6 kcal/mol (Schrödinger 2020) [31] is rather small and can likely be attributed to numerical error and/or changes in the protein preparation workflow in Maestro.

The docking analysis of the compounds identified in the fragment screen and the redocking of glyoxal bisulfite to the crystallographic holo-structure in the presence of R65 and R76 was performed with Maestro (Schrödinger release 2024r3). Additional receptor grids centered on the $NADP^+$-binding site in the presence and absence of docked glyoxal bisulfite and the G3P-site in the presence of docked R65 or R76 were generated.

Compound library generation

Inhibitor candidate libraries were created by using a combination of computational screening tools. The ENAMINE RealSpace chemical space was screened using the RealSpace Navigator software (BiosolveIT GmbH, Sankt Augustin, Germany). Each run was set to generate 1000 compounds, including virtual compounds generated from a database of known reactions with a chance of successful synthesis ≥80%. Compounds generated this way are indicated by the prefix "RSN_" followed by the template compound ("G3P:" glyceraldehyde-3-phosphate, "SuccA:" succinic acid and "Ch:" chloral hydrate) in Supplementary table S1.

A previously customized library of negatively charged ENAMINE and SPECS compounds for identification of SARS-CoV2 protease inhibitors ([40], provided by Dr. Goutam Mukherjee) was prescreened using the RASPD+ method [41] with default parameters, using all available regression models and no customized cutoffs. To filter the results, a customized dual-filtering pipeline was written in the R language for statistical computing [42], which has been made available on the RASPD+ GitHub page (https://github.com/HITS-MCM/RASPDplus). Here, only the first filter criterion was applied, namely that a compound must score within the best quartile of each regression model's score distribution. The set of input inhibitor-candidates was expanded by applying the "virtual libraries" machine learning method [43]. Default parameters were applied to generate extensive libraries of SMILES strings of novel compounds. The inhibitors created in this way are indicated by the source "virtual libraries" in Supplementary table S1.

Lastly, screening for compounds that can interact with both the active site and the vestibule region was based on the generation of a virtual probe molecule. While screening proposed inhibitors of the SARS-CoV2 proteases [44] on GapN from *S. pyogenes* with the aim of identifying oxyanion-hole binders, we noticed that the compound labetalol bound to the vestibule region without entering the active-site (Suplementary Figure S1), albeit with a poor docking score of −3.8 kcal/mol. In this pose, two arginine-residues, R103 and R283, at

the entry region to the substrate-binding site coordinate the labetalol hydroxyl group. In order to functionalize this group to bind one of the smaller active-site inhibitor candidates by an *in silico* esterification reaction, we used Maestro [39] to attach a docked pose of succinic acid to labetalol, which resulted in contacts with both regions of the binding site. Subsequently, this compound was used as input for RASPD+ and RealSpaceNavigator to generate a chemical compound library entitled "library II" in Supplementary Table S1.

Preparation of putative GapN inhibitors

Compounds 8, 9, and 29 were obtained from Merck KGaA (Darmstadt, Germany); compounds 11, 12, and 13 from Molport SIA (Riga, Latvia); and compounds 18 and 32 from BLD Pharmatech Ltd. (Shanghai, China). The remaining 24 compounds were purchased from ENAMINE Ltd. (Kyiv, Ukraine). Only for some compounds solubility information was available. However, most compounds could be dissolved to a final concentration of 100 mM (1–13) or 200 mM (14–36) in 10 mM DMSO (Carl Roth GmbH&CoKG, Karlsruhe, Deutschland). Compound 6 was dissolved in 20 mM DMSO. Compounds 7, 12, 13, 14, 27, 28, and 30 could not be dissolved in up to 20 mM DMSO and were therefore excluded from testing, leaving 25 compounds for screening. Ultra-low-molecular-weight compounds R16, R40, R65, and R76 were ordered from ENAMINE Ltd. (Kyiv, Ukraine) and dissolved to a final concentration of 200 mM in 10 mM DMSO. For all experiments, controls containing the respective final concentration of DMSO are noted in the respective figure legend.

Heterologous expression and purification of GapN and GapDH

For heterologous expression of *S. cristatus* GapN, chromosomal DNA of *S. cristatus* ATCC 51100 served as the template for the PCR amplification of *S. cristatus gapN* gene (primers 5'CCCGAATTCAAGCAATATA AGAACTAC-3' and 5'GGGCCATGGTTATTTCACA TCAAAC-3') with the Phusion™ High Fidelity PCR Kit (Thermo Scientific, Waltham, United States). The resulting PCR fragment was ligated into the pASK-IBA7 vector (IBA GmbH, Göttingen, Germany) system via EcoRI and NcoI restriction sites. The correct insertion of the PCR product was confirmed by Sanger sequencing. *E. coli* BL21 (DE3) cells were transformed with the recombinant vector pASKIBA7_ScrGapN. For the production of *S. pyogenes* GapN (SpyGapN) and *S. pyogenes* GapDH (SpyGapDH), previously published strains were used [31].

The heterologous expression and purification of *S. cristatus* GapN (ScrGapN), SpyGapN and SpyGapDH via StreptTactin affinity chromatography was carried out as previously described [31]. The purified SpyGapDH was dialyzed overnight in PBS (pH 7.4) while SpyGapN and ScrGapN were dialyzed in 0.1 M citric acid (pH 6.0) to prepare the enzymes for subsequent activity assays.

Measurement of GapN and GapDH activity

The specific GapN and GapDH activity was measured as described elsewhere [45] with some modifications. To account for the high pH sensitivity of SpyGapN (Supplementary Figure S2), the assay mixture was based on 200 mM Tricine buffer (pH 8.5) and contained 0.5 mM dithiothreitol, 10 mM $NADP^+$ (Carl Roth GmbH&CoKG, Karlsruhe, Deutschland), 2 mM DL-glyceraldehyde 3-phosphate (DL-G3P) (Sigma-Aldrich GmbH, Taufkirchen, Deutschland), 10 mM citric acid (pH 6.0), and 50 nM purified protein. The reaction was started by adding DL-G3P. The reduction of $NADP^+$ to NADPH was detected by measuring the absorption at 340 nm in a spectrophotometer for 15 min. To measure the GapDH activity, the assay mixture contained 200 mM Tricine buffer (pH 8.5), 0.5 mM dithiothreitol, 10 mM NAD^+ (Sigma-Aldrich GmbH, Taufkirchen, Deutschland), 10 mM $Na_2HPO_4^{2-}$ (pH 8.5), 2 mM DL-G3P, 2.5% (v/v) PBS (pH 7.4), and 50 nM purified protein. The reaction was started by adding DL-G3P. The reduction of NAD^+ to NADH was detected by measuring the absorption at 340 nm using a SpectraMax 380 Plus microplate reader for up to 30 min. As controls, the assays were carried out without the addition of protein sample and without the addition of DL-G3P, respectively. Enzyme activity was calculated using the Lambert–Beer equation and expressed in units per milligram of total protein (U/mg), where one unit is defined as the formation of 1 µmol NADPH or NADH per minute.

Time-kill assay

For compounds providing a decrease in SpyGapN enzyme activity by ≥ 50%, time-kill kinetics of *S. pyogenes* M49 591 were monitored. For this, overnight cultures of *S. pyogenes* were diluted in 200 mM Tricine saline buffer (137 mM NaCl, 4.7 mM KCl, 200 mM Tricine, pH 8.0) with 20% (v/v) BHI to 10^5 CFU/ml. To assess bacterial susceptibility, the compounds were mixed 1:9 with bacterial suspensions of the respective

strains and incubated for 24 h at 37°C rotating at 7 rpm. Subsequently, viable counts were determined by plating serial dilutions after 2, 4, 6, 8, and 24 h on THY agar plates.

Crystallization and structure determination

Since the wild-type structure (PDB entry 7PKJ) displayed additional electron density at the active site C284, potentially due to a covalent modification with an unidentified molecule, the C284S variant was used for the crystallographic studies. For co-crystallization, this variant was mixed at a concentration of 8 mg/mL in PBS with 0.5 mM G3P at 4°C. Afterward, 1 mM $NADP^+$ was added. The final crystals were derived from a fine screening campaign in 0.01 M PBS buffer pH 7.4, 0.160–0.185 M $(NH_4)_3$-citrate and 18–21% *(w/v)* polyethylene glycerol 3350 by mixing 1 µL of protein sample with 1 µL of mother liquor in hanging-drop vapor diffusion experiments conducted at 20°C. After 75 days, crystals were obtained, which were transferred into a cryoprotective solution with 0.5 mM G3P and 1 mM $NADP^+$. As a cryo-protectant, 25% (*v/v*) glycerol was added.

Crystals for fragment soaking experiments were prepared by hanging-drop vapor diffusion at 20°C. Again, the C284S mutant was used at a concentration of 2.5 mg/mL in 0.02 M HEPES buffer pH 8.5 containing 0.125 M NaCl. The corresponding mother liquor consisted of 0.1 M BisTris buffer pH 6.7, 0.2 M Li_2SO_4 and polyethylene glycol 3350 (21–22 % (*w/v*)). Native crystals were obtained by mixing 2 µL of protein solution with 1 µL mother liquor. After 4–8 days, crystals formed, which were used for soaking experiments. For soaking, the solutions were prepared with the same concentrations as the mother liquor and, depending on the behavior of the crystals during the test soaking experiments, additionally 1 M R16, 0.5 M R40, and R65 or 0.333 M R76 were added for 10 s. Afterward, the crystals were washed in mother liquor and transferred to mother liquor supplemented with 25% (*v/v*) glycerol as cryoprotectant.

Diffraction data for GapN with G3P and $NADP^+$ were collected at DESY (EMBL, Hamburg, Germany) on beamline P13 of the PETRA III storage ring with an Eiger 16 M detector (Dectris) at a wavelength of λ = 0.976 Å. Datasets with the fragments were collected at beamline ID30B (ESRF-EBS, Grenoble, France) with an Eiger2x9M detector (Dectris) at a wavelength of λ = 0.976 Å (R16), beamline BL14.1 at BESSY (Helmholtz-Zentrum, Berlin, Germany) with a Pilatus3 S 6 M detector (Dectris) at a wavelength of λ = 0.918 Å (R40, R65), and DESY (EMBL, Hamburg, Germany) on beamline P13 of the PETRA III storage ring with an Eiger 16 M detector (Dectris) at a wavelength of λ = 0.689 Å (R76). The temperature during data collection was always 100 K. Data were processed with the program *X-Ray detector software* (XDS) [46] for indexing, integrating, and scaling as well as Staraniso [47] for taking anisotropic diffraction into account. The structure of the GapN-$NADP^+$-G3P complex was solved by molecular replacement with the program Phaser (CCP4) with the already existing structure of GapN C284S from *S. pyogenes* (PDB entry: 7PKC) as search model. FreeR flags were generated with the program FreeRflag (CCP4) [48], and initial refinement was done with Refmac5 (CCP4) [49], followed by manual model building in Coot [50]. Further refinement steps were done with Phenix.refine [51] and the resulting structure was evaluated with MolProbity [52]. For the fragments, the refinement was directly initiated by model building in Coot and completed as described above.

Statistical analysis

The number of biological replicates (*n*) and the tests used to determine statistical significance for each data set are indicated in the respective figure captions. Statistical analyses were performed using GraphPad Prism 10 software.

Results

In silico screening identifies potential GapN inhibitors

A virtual screening pipeline based on the native substrate of GapN, G3P, as well as diverse known inhibitors of related proteins, including mitochondrial aldehyde dehydrogenase (inhibitor: chloral hydrate) and mitochondrial succinate-semialdehyde dehydrogenase, was used to generate a selection of candidate inhibitors. Since no crystallographic structure of GapN from *S. pyogenes* was available at the time, we used our previously published homology model [31] based on GapN from *S. mutans* (PDB-ID: 1Q1) [36] as the target for molecular docking. Several compound collections were constructed by a combination of library screening and generation of novel compounds. We used a selection of various discovery and generative tools in different combinations yielding a library of compounds which were screened by docking (see "Materials and methods" for details). Briefly, potential inhibitors were identified through three different means: (1) chemical space screening with the

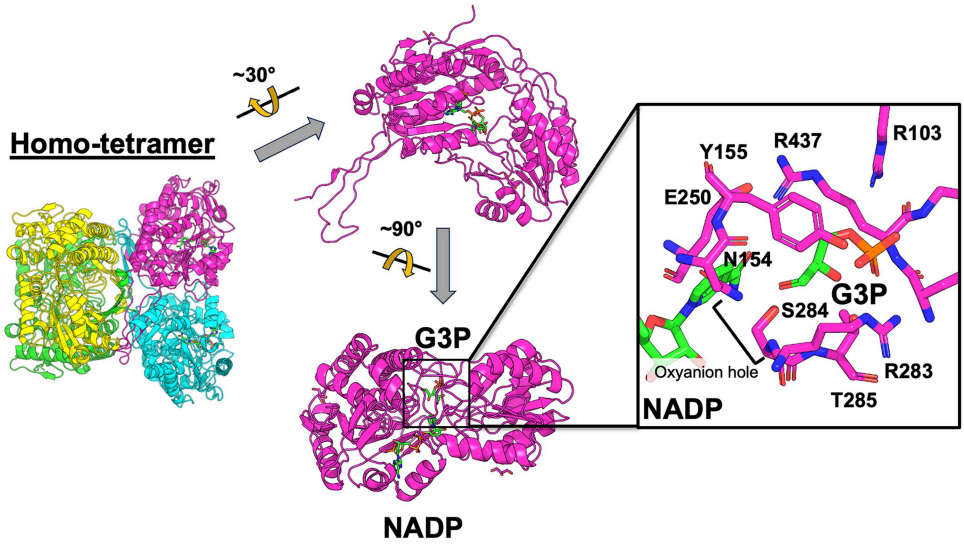

Figure 1. Overview of the crystallographic holo-structure of SpyGapN. The monomer with both G3P and NADP+ bound is colored magenta, G3P and NADP+ are displayed in green "sticks" representation. The two binding sites are located in the center of the globular domain with the openings for either ligand being located at opposite faces (as indicated in the "top view" panel). The inset highlights the active site with important residues depicted in stick representation. The two sites merge at the oxyanion hole formed by the main chain N-atoms of N154 and S284 (mutated from cysteine in the wild-type enzyme).

ENAMINE REALSpace Navigator Software (BiosolveIT GmbH, Sankt Augustin, Germany), (2) screening of a previously pre-selected database of ENAMINE and SPECS compounds [40] and prescreening using the RASPD+ tool [41], and (3) generation of novel compounds using the "virtual libraries" machine learning method [43]. Intermediate results from one method were used as input for the other methods in diverse combinations. Out of a total of 95,805 docked compounds, 100 fulfilled the criterion of a docking score < 7 kcal/mol and passed visual inspection of the docking pose. An overview of the position of the binding site within the protein is given in Figure 1.

We found that optimal binding to the active site of GapN requires the presence of negatively charged (acidic) or highly polar groups at both ends of a linear C_3-C_5 scaffold, which in some compounds was part of a larger cyclopropane or cyclopentane ring. If positioned linearly within the active site between the $NADP^+$ cofactor and the entry region, these groups optimally exploit both the oxyanion hole, formed by C284 and N154, as well as the highly basic entry region, formed by R103, R283, and R437, which coordinates the phosphate moiety of G3P in the homology model. Additional polar groups between the two ends help to stabilize the pose through hydrogen-bonds with the polar residues Y155 and T285. Thus, succinic acid proved to be the most effective template for the identification of such compounds due to its optimal fit and remarkably simple chemical nature.

In comparison, binding to the vestibule region, in addition to the active site, required a polar link to a polycyclic, amphiphilic moiety, most often either an ester or an amide linkage. Binding of the outer moiety to the surface of the vestibule region is mostly stabilized by nonspecific hydrophobic interactions. We found that most of the compounds that bind to both regions with reasonable docking scores are based on a sulfonic acid amide scaffold with a highly polar group pointing into the binding site and a polyheterocyclic group in the vestibule.

Of the 100 identified compounds with docking scores ≤ −7 kcal/mol and reasonable docking poses, 32 were available for purchase. These 32 compounds were selected for *in vitro* testing where it was found that only 25 compounds displayed sufficient solubility for experimental testing (Suplementary Table S1). Interestingly, out of these, only compound four fulfilled the criterion of a docking score ≤ −7 kcal/mol with both its (R)- and (S)-stereoisomers. As the initial library generation procedure did not consider stereochemistry, all possible stereoisomers were docked. As most experimentally tested compounds were present as racemic mixtures, a direct comparison between docking and experiment was not possible in all cases.

Glyoxal bisulfite inhibits GapN activity

The 25 putative GapN inhibitors were analyzed for their effects on the activity of purified SpyGapN. For this purpose, 8 mM of the compounds were added to

the standard GapN activity assay mixture, leading to a fourfold molar excess of each compound over the natural substrate G3P. E4P, a metabolite of the nonoxidative part of the pentose phosphate pathway that was previously identified to inhibit SpyGapN [31,53], was used as a control. A dose-dependent inhibition of SpyGapN was determined for 0.05–2 mM E4P (Supplementary Figure S3A) with more than 85% reduction of SpyGapN activity at 2 mM.

Significant inhibition of SpyGapN was only achieved by two of the compounds tested, namely compound 26 (glyoxal bisulfite) and compound 32 ((ethoxyoxydophosphanyl) formate), which led to a reduction in activity of approximately 50% and 25%, respectively (Figure 2). The remaining compounds derived from the *in silico* screening did not reduce the SpyGapN activity significantly in the tested concentration. Compounds 1 ((2-(hydroxyamino)-2-oxoethyl) phosphonic acid) and 25 (2-hydroxyglutarate) even caused an apparent increase in SpyGapN activity. It remains unclear if this is a consequence of these compounds acting as alternative substrates or if they act as allosteric modulators of SpyGapN by an unknown mechanism. For glyoxal bisulfite, which proved to be the most promising SpyGapN-inhibiting compound, the dose dependence of inhibition was examined by measuring SpyGapN activity in the presence of 2–20 mM (Figure 3(A)), resulting in a decrease in SpyGapN activity of more than 90% at the highest concentration compared to the untreated control.

Next, we investigated whether glyoxal bisulfite affects G3P-binding enzymes in general or specifically inhibits SpyGapN. To this end, the activity of purified SpyGapDH and *Streptococcus cristatus* GapN (ScrGapN) was measured in the presence of 8 mM glyoxal bisulfite (Figure 3(B)). It was found that the compound also had inhibitory effects on these two enzymes. It impaired the activity of SpyGapDH to a similar extent as to SpyGapN and reduced the activity of ScrGapN even more efficiently by about 70%. The PPP intermediate E4P was used as a control and did not significantly reduce SpyGapDH activity (Supplementary Figure S3B).

Since glyoxal bisulfite is predicted to compete with G3P for the G3P binding site, the impact of the compound on Michaelis–Menten kinetics of SpyGapN for

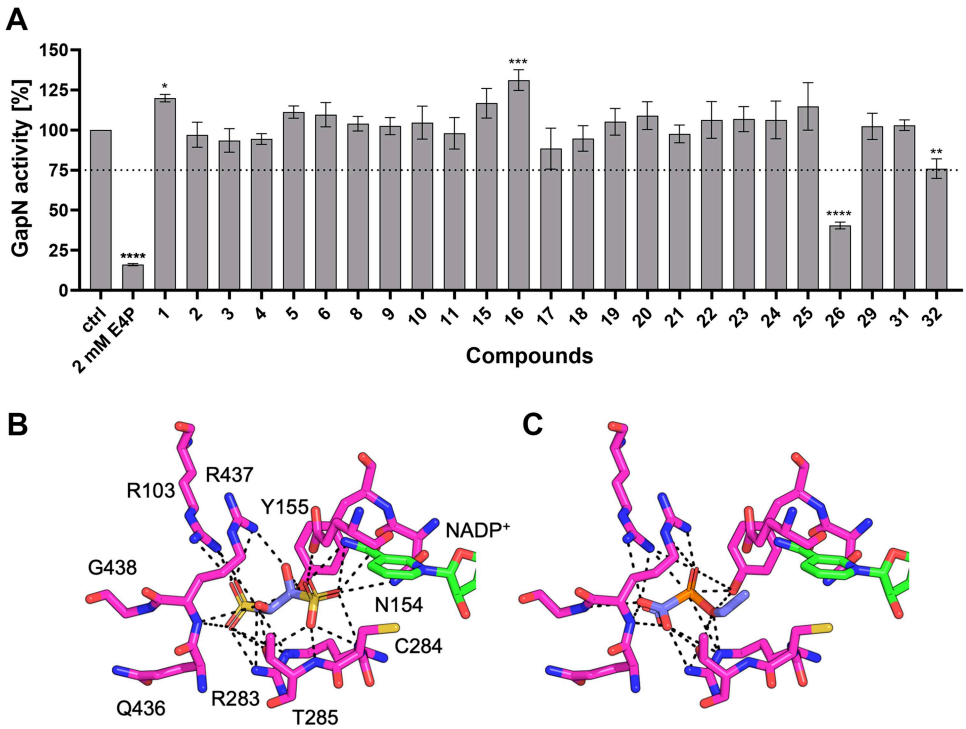

Figure 2. Influence of potential inhibitors on SpyGapN activity. (A) specific activities measured in the presence of 8 mM inhibitor are shown relative to the specific activity of the control (1 mM DMSO) without inhibiting compound. Erythrose 4-phosphate (E4P) was used as a control inhibitor. Inhibitor numbers match the numbers given in Supplementary table S1. Dashed line indicates 75 % enzyme activity compared to the untreated control, which was set as the cutoff for further analysis of the inhibitors. Mean values and standard deviations; $n = 3$; *$p < 0.05$, ***$p < 0.001$, ****$p < 0.0001$ vs. control (one-way ANOVA followed by Dunnett's multiple comparisons test). (B) Docking poses of compound 26 (glyoxal bisulfite) and (C) compound 32 (ethoxyoxydophosphanyl)formate identified to have a significant inhibitory effect. The structures are colored by atom-type with the carbons in green for the nicotinamide of NAD+, magenta for the protein residues in the binding site, and blue for the docked compounds. Polar interactions are shown by black dashed lines. The compound index is given beneath each pose.

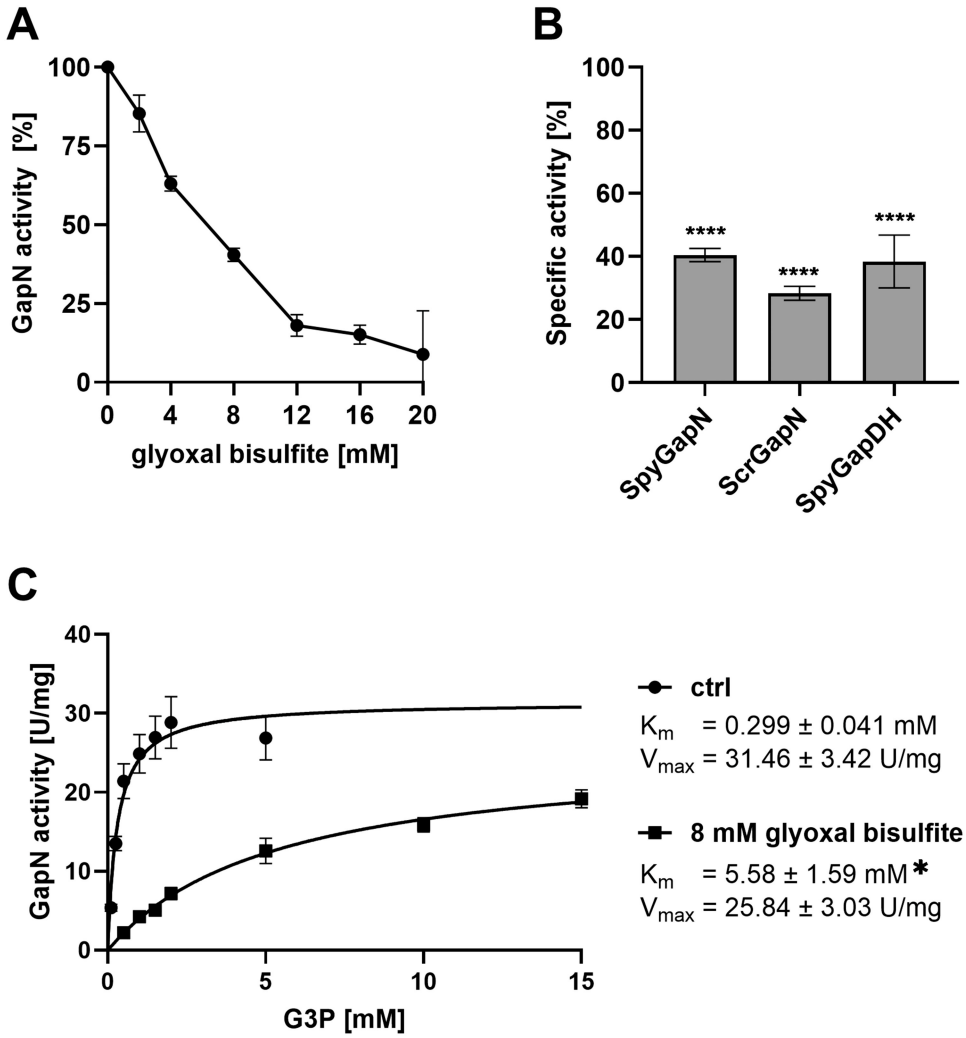

Figure 3. Effect of glyoxal bisulfite on GapN activity. (A) dose dependency of the effect of glyoxal bisulfite on SpyGapN activity and (B) effect of 8 mM glyoxal bisulfite on SpyGapN, ScrGapN, and SpyGapDH. Specific activities measured at the indicated inhibitor concentrations are shown relative to the specific activity of the control (1 mM DMSO) without inhibiting compound. ****$p < 0.0001$ vs. control (one-way ANOVA followed by Dunnett's multiple comparisons test). (C) Michaelis–Menten kinetics for G3P of SpyGapN in the absence and in the presence of 8 mM glyoxal bisulfite. *$p < 0.01$ vs. control (two-tailed Student's *t*-test). Mean values and standard deviations of $n = 3$ biological replicates.

G3P was investigated. For this purpose, SpyGapN activity was measured in the absence and in the presence of 8 mM glyoxal bisulfite and G3P concentrations ranging from 0.5 to 15 mM (Figure 3(C)). In the presence of glyoxal bisulfite, the maximum reaction rate (V_{max}) decreased by about 20% and the Michaelis constant (K_m) for G3P increased about 20-fold from 0.3 to 5.4 mM.

Crystal structure of the ternary GapN-NADP$^+$-G3P complex

To obtain a structure showing the cofactor nicotinamide adenine dinucleotide phosphate (NADP) and its substrate G3P in complex with GapN, a search for different crystallization conditions was conducted since the presence of sulfate molecules in the published crystallization conditions was considered to be incompatible with the binding of the cofactor and the substrate. After the identification of novel crystallization conditions (see "Materials and methods"), a structure of the GapN C284S variant in complex with NADP$^+$ and G3P (PDB entry 9RAZ) was derived at a resolution of 1.3 Å (Figure 4(A-–C)). Data collection and refinement statistics are summarized in Tables 1 and 2. Surprisingly, this structure only showed binding of the cofactor to two monomers of the tetramer. This half occupancy was observed for both tetramers present in the asymmetric unit, resulting in four monomers containing NADP$^+$ and four monomers being present in the apo-state. The cofactor-containing subunits also showed electron density for the substrate; however, the electron density was often fragmented and G3P was therefore modeled in only one of the eight subunits.

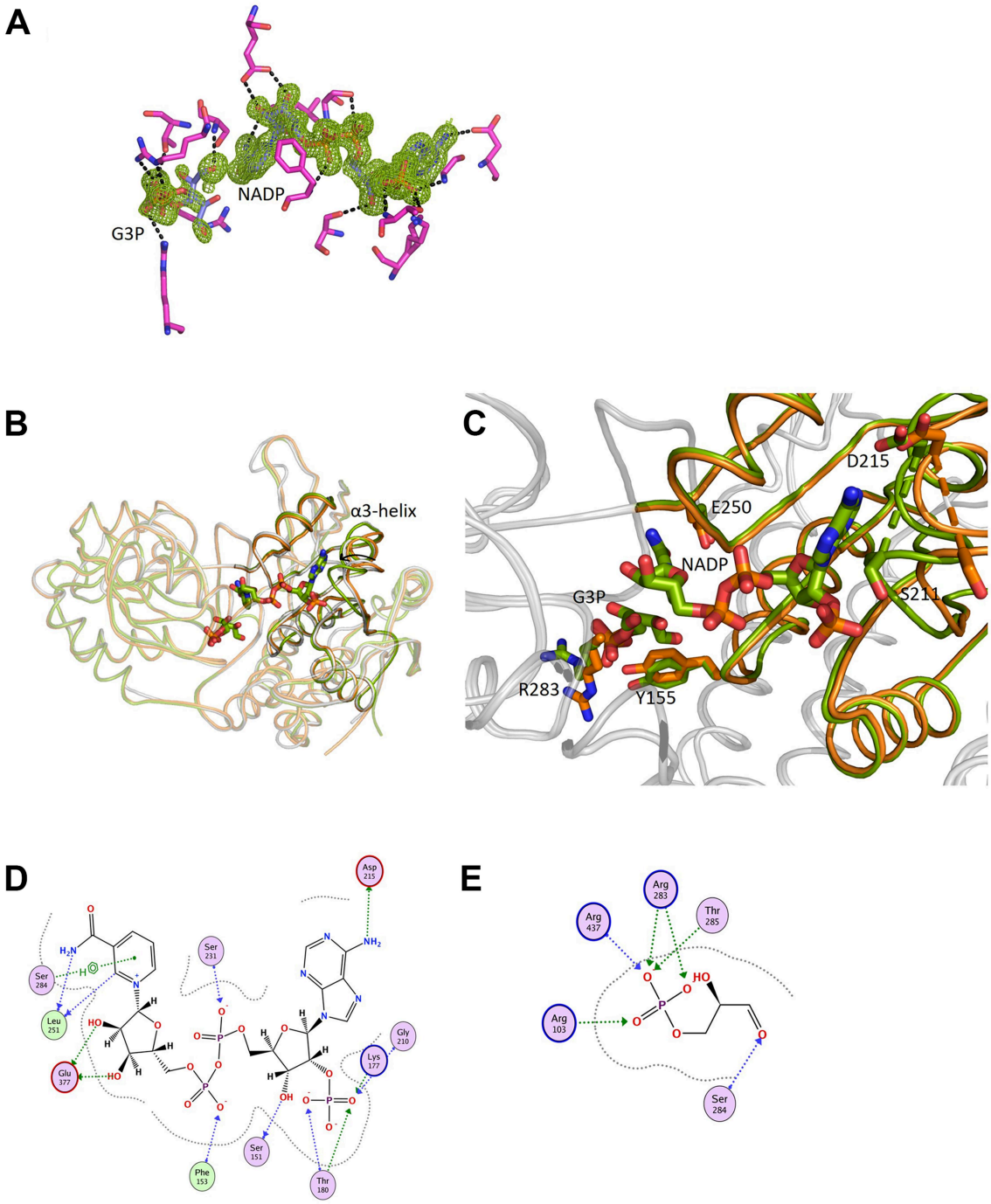

Figure 4. Structural features of the ternary GapN-G3P-NAPD$^+$ complex. (A) F_o-F_c difference electron density map (green mesh) contoured at three times the RMS deviation after omitting NADP$^+$ (blue C-atoms) and G3P (green C-atoms) from the model with interacting residues (magenta C-atoms). (B) Superimposition of monomer F with G3P and NADP$^+$ (green) and monomer D (apo-state in orange) from the GapN-G3P-NADP$^+$ complex as well as monomer a (gray) from the GapN apo-structure (PDB entry 7PKC). (C) Zoom-in into the cofactor binding site comparing the structures of monomer F (green) and monomer D (orange) from the GapN-G3P-NAPD$^+$ complex highlighting the Rossmann fold. (D) Schematic diagram of the interactions between GapN (chain F) and NADP$^+$. Legend: pink circle without frame color: polar amino acid; pink circle with red frame: acidic amino acid; pink circle with blue frame: basic amino acid; green circle: hydrophobic amino acid; blue arrow: backbone acceptor/donor; green arrow: sidechain acceptor/donor; red dashes: solvent contact. (E) Schematic diagram of the interactions between GapN (chain F) and G3P. Interaction types are indicated as described in (D).

Table 1. Crystallographic data collection statistics.

	C284S NADP$^+$+G3P	Fragment R16	Fragment R40	Fragment R65	Fragment R76
Beamline	PETRA III P13	ID30B	BL14.1	BL14.1	PETRA III P13
Space group	P1	P1	P1	P1	P1
Unit cell dimensions a, b, c (Å), α, β, γ (°)	97.15 97.44 100.71 77.06 78.19 68.92	98.52 99.58 104.16 77.66 75.94 67.67	97.15 97.15 100.70 76.94 77.99 68.28	97.76 98.95 103.03 78.04 75.63 67.01	97.56 98.97 103.23 77.68 75.95 67.49
Wavelength (Å)	0.9763	0.9763	0.9184	0.918400	0.689
Resolution limits (Å)	48.62–1.38	47.74–1.61	46.58–1.57	44.22–1.77	47.29–1.44
Total/unique reflections	1,849,387/528,737	1,443,277/437,149	1,586,722/430,858	1,131,463/310,076	1,871,493/497,136
Spherical data completeness (%)	76.39 (19.08)	70.57 (4.11)	82.24 (16.59)	67.54 (8.30)	50.50 (6.70)
Elliptical data completeness (%)	91.92 (62.41)	91.6 (64.0)	90.2 (60.0)	87.4 (57.8)	85.0 (53.1)
$CC_{1/2}$	0.9978 (0.4970)	0.998 (0.485)	0.999 (0.599)	0.993 (0.238)	0.999 (0.740)
[a]R_{merge}	0.054 (0.811)	0.075 (1.035)	0.070 (0.857)	0.1738 (2.187)	0.060 (0.530)
[b]R_{pim}	0.033 (0.518)	0.048 (0.686)	0.042 (0.5044)	0.105 (1.315)	0.036 (0.321)
[c]< I/sigI>	10.33 (1.53)	10.20 (1.12)	12.46 (1.50)	6.64 (0.61)	9.5 (1.7)
Diffraction limits (Å)	1.44 1.38 1.59	1.55 1.82 1.75	1.67 1.63 1.57	1.77 2.27 1.81	1.50 1.93 1.82

[a]$R_{merge} = \Sigma_{hkl}\Sigma_i |I_i - \langle I \rangle| / \Sigma_{hkl}\Sigma_i I_i$ where I_i is the i^{th} measurement and $\langle I \rangle$ is the weighted mean of all measurements of I.
[b]$R_{pim} = \Sigma_{hkl} 1/(N-1)^{1/2} \Sigma_i |I_i(hkl) - I(hkl)| / \Sigma_{hkl}\Sigma_i I(hkl)$, where N is the redundancy of the data and $I(hkl)$ the average intensity.
[c]$\langle I/\sigma I \rangle$ indicates the average of the intensity divided by its standard deviation.
Numbers in parentheses refer to the respective highest resolution shell (1.48–1.38 Å, 1.67–1.61 Å, 1.63–1.57 Å, 1.83–1.77 Å, and 1.55–1.5 Å, respectively).

Table 2. Crystallographic refinement statistics.

	C284S NADP$^+$+G3P	Apo R16	Apo R40	Apo R65	Apo R76
PDB entry	9 RAZ	9RB1	9RAS	9RAU	9RAV
Resolution limits (Å)	48.62–1.38	47.74–1.61	46.58–1.57	44.22–1.77	47.24–1.5
[a]R_{work}	0.1541 (0.2594)	0.1572 (0.2745)	0.1548 (0.2187)	0.1770 (0.2404)	0.1911 (0.3926)
[b]R_{free}	0.1792 (0.2900)	0.1932 (0.3197)	0.1913 (0.2744)	0.1801 (0.2283)	0.1916 (0.3854)
Coordinate error (Å)	0.13	0.14	0.17	0.21	0.17
rms deviations in					
Bond lengths (Å)	0.006	0.005	0.005	0.004	0.008
Bond angles (°)	0.743	0.72	0.75	0.60	0.71
Dihedral angles (°)	12.33	12.63	12.61	12.69	12.08
Planar groups (Å)	0.008	0.006	0.007	0.007	0.007
[c]Ramachandran statistics (%)	97.46/2.46/0.08	97.43/2.57/0.00	97.80/2.20/0.00	97.30/2.67/0.03	97.59/2.41/0.00
Clashscore	2.38	2.08	3.32	2.02	2.92
Number of atoms	33,909	33,371	34,456	31,879	33,308

[a]$R_{work} = \Sigma_{hkl} ||F_o| - |F_c|| / \Sigma_{hkl}|F_o|$ where F_o and F_c are the observed and calculated structure factor amplitudes. Numbers in parentheses refer to the respective highest resolution shell (1.48–1.38 Å, 1.67–1.61 Å, 1.63–1.57 Å, 1.83–1.77 Å, and 1.55–1.5 Å).
[b]R_{free} same as R for 2.52%, 5.00%, 5.00%, 5.00%, and 4.85% of the data randomly omitted from the refinement.
[c]Ramachandran statistics were calculated with MolProbity in PHENIX.

NADP$^+$ is bound in a pocket formed by the Rossmann fold (residues 7–13 and 144–251) and the catalytic domain (residues 252–448), with the adenosyl moiety being placed on top of the β-sheet of the Rossmann fold and bound between two α-helices. The nicotinamide moiety reaches into the catalytic domain, which is coordinating the cofactor through residues of the loops. NADP$^+$ is exclusively ligated by a single monomer with no residues being contributed from an adjacent subunit (Figure 4(D)). A figure schematically summarizing the interactions was generated with MOE (Molecular Operating Environment, 2023 Chemical Computing Group ULC, 910–1010 Sherbrooke St. W., Montreal, QC H3A 2R7) [27]. NADP$^+$ forms polar interactions with residues 151, 153, 177, 180, 215, 231, and 251 from the Rossmann fold and the active site residues 284, 377, and 437. Interactions can be observed between L251 and S284, replacing the active site cysteine, to the nicotinamide moiety, E377 to the 2'-OH and 3'-OH groups of the ribose, S231 and F153 to one of the phosphates in the pyrophosphate linker, S151 and T180 to the ribose of the adenosine as well as K177, T180, and G210, which coordinate the phosphate group attached to the adenosine ribose. Finally, D215 is coordinating the adenosyl group with its side chain.

Despite the presence of 0.5 mM G3P, satisfactory electron density for the G3P substrate (Figure 4(A)) could only be observed for one chain (chain F) out of all eight subunits, with residual densities being present in three additional subunits (chains A, B, and E). The G3P in the F-chain was modeled with two conformations, which almost coincide at the position of the phosphate group and diverge most prominently at the aldehyde function at the opposite end of the molecule. The subunits displaying density for G3P are the same subunits in which the NADP$^+$

cofactor could be visualized; however, the quality of the electron density precluded model building of G3P in these chains. The phosphate group of G3P appears to serve as an anchor point, in agreement with its virtually unchanged position in the two conformations of G3P. This fixation of the phosphate group appears to be due to its multiple interactions with the guanidinium groups of R103 and R283. In addition, the side chain of T285 and the backbone nitrogen of R437 engage in hydrogen bonds with the phosphate group (Figure 4(E)). As stated above, S284 was substituted for the active site C284 and, during catalysis, a covalent bond would be formed between the substrate and the SH-group of C284.

Docking poses to the homology model and to the crystallographic structure are comparable

Our *in silico* screening pipeline was based on a homology-model [8] (template: PDB-ID 1QI1 [36]), constructed before the crystal structure of the ternary GapN-$NADP^+$-G3P complex (PDB entry 7PKJ) from *S. pyogenes* became available. Despite a different conformation of R283 and a 180° rotation of the nicotinamide-ring of the NADPH-cofactor, we observed a qualitatively high agreement in both the pose of G3P (Supplementary Figure S4) and the docking scores of the 32 compounds (Supplementary Table S1). To assess the effects of the structural differences on the docking of the substrate G3P, we separately introduced the NADPH-rotation and the different conformation of R283 into the crystallographic structure. In both cases, the docking scores of −8.5 (NADPH-rotation) and −8.6 kcal/mol (altered R283 conformation) (best poses) were within 0.2 kcal/mol of the value for the unaltered structure (−8.7 kcal/mol). Additionally, the generated docking poses remained remarkably similar to the pose of G3P docked to the unaltered structure.

Crystallographic fragment screening identified four hits within functionally relevant regions of GapN

In parallel to the virtual screening approach, a crystallographic fragment screening campaign was conducted to identify first starting points for the development of GapN inhibitors. For screening, the methodology reported by O'Reilly *et al.* [54] was chosen. This library consists of 80 chemically diverse, ultra-low-molecular-weight compounds (5–7 heavy atoms) that were used in high-concentration aqueous soaks up to 1 M, which resulted in four unambiguous hits.

The ultra-low-molecular-weight compound R16 (2-cyanoacetamide, PDB entry 9RB1) is coordinated via its amide NH_2-moiety to the backbone of T285 and a sulfate ion (Figure 5(A,E)), while its carbonyl group interacts via a water-bridged hydrogen bond with S284 and N154 and the nitrile group forms a hydrogen bond to R437. By interacting with the aforementioned amino acids, the fragment adopts a slightly bent conformation at the β-carbon with a torsion angle of 31.7° ± 4.3°. This fragment is present with full occupancy in all subunits of both tetramers based on its average B-factor being very similar to those of the surrounding atoms.

The ultra-low-molecular-weight compound R40 (imidazoline-2,4-dione, PDB entry 9RAS) was identified three times in four subunits (Figure 5(B,F)) occupying distinct pockets within the binding site, while it was present twice in the remaining four monomers. In the following, we will describe the location of all three copies of compound R40. The first site is located in the substrate-binding pocket where it is coordinated by residues R103 and R283, where the phosphate group of G3P was found in the substrate-bound ternary complex. Additionally, the backbone nitrogen of G438 coordinates the compound via a polar interaction. The second binding site partly overlaps with the position of the nicotinamide moiety in the ternary complex, and the compound engages in hydrogen bonds with residue R437. A water molecule bridges the interaction with the third binding site connecting the hydroxyl/carbonyl group (enol-keto tautomerization) of the compound. The third binding site almost coincides with the position of the ribose attached to the nicotinamide ring. In this location, the compound interacts via ππ stacking interactions with F379 and a hydrogen bond to E377.

The ultra-low-molecular-weight compound R65 (pyrimidine-5-amine, PDB entry 9RAU)) is stabilized by a BisTris molecule, a remnant of the buffer solution (Figure 5(C,G)). Interestingly, the buffer molecule could only be visualized in the presence of compound R65. The compound engages in a hydrogen bond with the side chain of E377 and a water molecule, which, in turn, engages in hydrogen bonds with the main-chain oxygens of G230 and L251. Furthermore, the compound is stabilized by ππ stacking interactions with F379, as described before for the third copy of compound R40.

Finally, the ultra-low-molecular-weight compound R76 (4-hydroxypyridazine, PDB entry 9RAV) binds in the same manner as the third copy of compound R40 as well as compound R65 to the pocket where the nicotinamide of $NADP^+$ is located, engaging in a hydrogen bond with E377 and ππstacking interactions with F379.

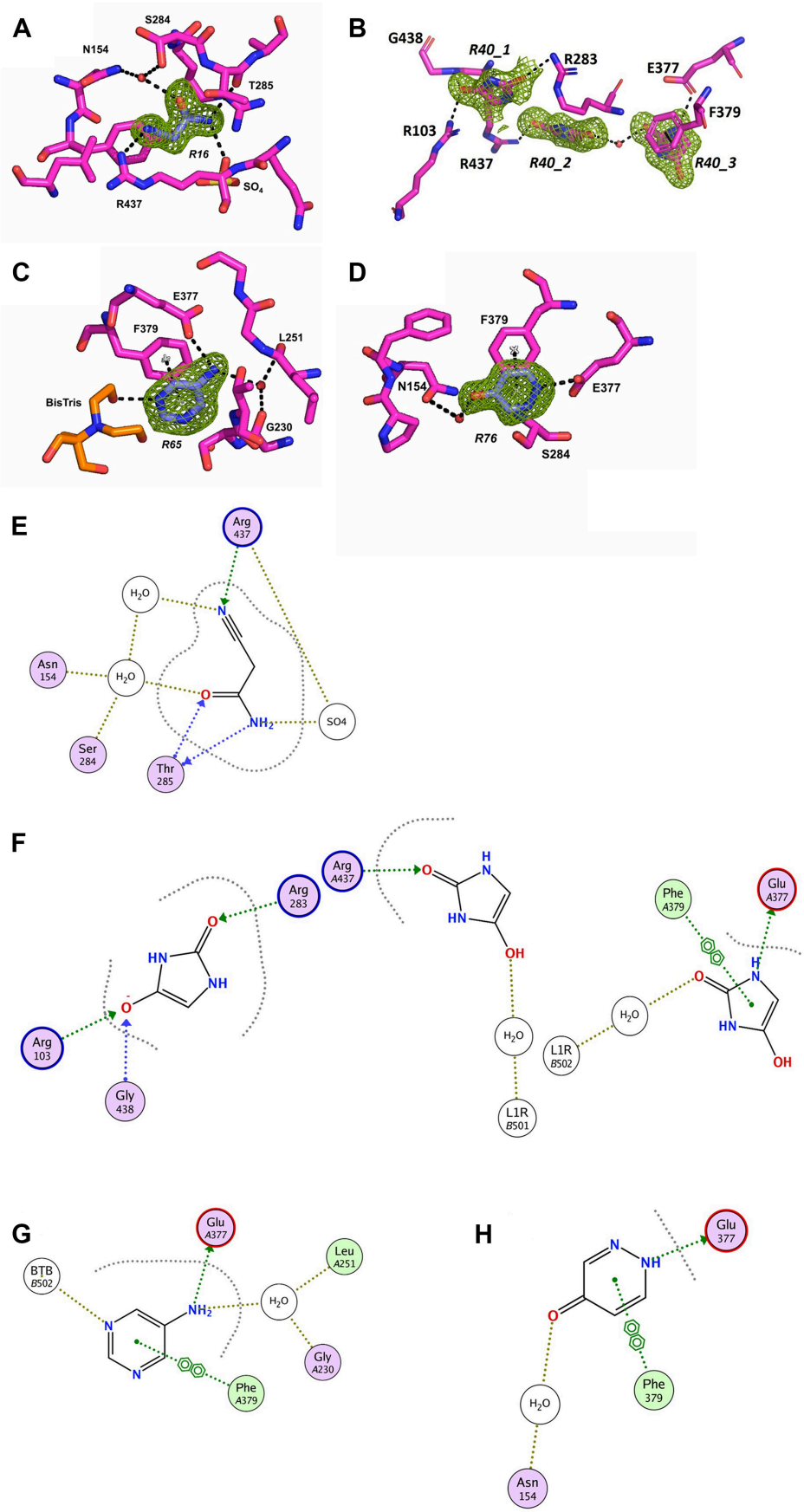

Figure 5. GapN structures with compounds identified in the fragment screen. (A–D) F_o-F_c difference electron density maps (green mesh) contoured at three times the RMS deviation after omitting R16 (A), R40 (B), R65 (C), and R76 (D) from the model surrounded

In contrast to the other ultra-low-molecular-weight compounds, there is an additional water-mediated contact from the hydroxyl-group of compound R76 to the side-chain oxygen of N154 (Figure 5(D,H)).

All four ultra-low-molecular-weight compounds were successfully computationally docked to the G3P-bound holo structure in very similar poses to their crystallographic structures (Supplementary Figure S5) despite yielding less favorable docking scores than G3P or the inhibitor-candidates due to their smaller size and lower number of interactions (Table 3). For R40, only the location of the R40_1 copy was successfully replicated. The compounds docking to the active site displayed a more specific binding mode close to the crystallographic pose, whereas docking of R65 and R76, which are located in the $NADP^+$ site in the crystal structures, also yielded *off-site* poses located in different regions of the binding site (Table 3).

The six binding sites derived from the four hits were all located in pharmacologically relevant regions, namely the pockets where the substrate G3P and the cofactor are bound as identified in the 1.4 Å structure (PDB entry 9RAZ) of the ternary complex reported in this manuscript (Figure 6). The active site is divided into two subsites in such a way that the cofactor binds to the enzyme from one side, with its nicotinamide ring being inserted into a funnel, which connects the two sites, while the substrate approaches the active site from the opposite direction via the vestibule. Three of the six binding sites are located on the cofactor side; specifically, they all closely overlap with each other and bind where the nicotinamide ribose is located. On the opposite side, the compounds do not coincide, with the two copies of R40 either overlapping with the phosphate of G3P or the aldehyde function of G3P and the amide of nicotinamide and R16 being located in between the two R40 sites.

Pyrimidine-5-amine and 4-hydroxypyridazine increase SpyGapN inhibition and antibacterial effects of glyoxal bisulfite

The inhibitory potential of R16, R40, R65, and R76 on SpyGapN was assessed in SpyGapN activity assays. Given their ultra-low molecular weight, 40 mM of each compound was used in the assay (Figure 7(A)). While R40 significantly increased SpyGapN activity, R65 and R76 caused a significant inhibition of the enzyme by about 42% and 16%, respectively. R16 did not cause a change in SpyGapN activity, which agrees with its best docking score being the least favorable out of the studied compounds and its average docking score being the second least favorable (Table 3).

As R65 and R76 were found within the $NADP^+$ binding pocket of SpyGapN, their impact on Michaelis–Menten kinetics of SpyGapN for $NADP^+$ was analyzed. SpyGapN activity was measured in the absence and in the presence of 40 mM pyrimidine-5-amine (R65) or 4-hydroxypyridazine (R76), respectively, with $NADP^+$ concentrations ranging from 0.025 to 2 mM (Figure 7(B)). In the presence of R65, the maximum reaction rate (V_{max}) decreased by about 50%, and the Michaelis constant (K_m) for $NADP^+$ was significantly decreased by approximately 30%. The presence of R76 reduced the maximum reaction rate (V_{max}) by about 20%, while the Michaelis constant (K_m) for $NADP^+$ remained unaffected.

Next, combinations of glyoxal bisulfite with pyrimidine-5-amine (R65) and 4-hydroxypyridazine (R76) were tested in SypGapN activity assays to assess potential combinatory effects. Combining 8 mM glyoxal bisulfite with 8 mM or 40 mM of either compound resulted in a further decrease in SpyGapN activity by 10–15% compared to glyoxal bisulfite alone (Figure 8). In both cases, this effect was dose dependent. With the Bliss independence model [55,56], the combination index of 8 mM glyoxal bisulfite and 40 mM pyrimidine-5-amine (R65) was calculated to be 1.03, indicating an additive effect. For the combination of 8 mM glyoxal bisulfite with 40 mM 4-hydroxypyridazine (R76), the combination index was calculated to be 0.9, indicating a slightly synergistic effect. Combinations of 4-hydroxypyridazine (R76) with the natural inhibitor E4P did not increase the inhibitory effect of the latter, while 40 mM of pyrimidine-5-amine (R65) added to the inhibitory effect of E4P (Supplementary Figure S3C).

To investigate the basis of these effects, we redocked glyoxal bisulfite to receptor grids based on the highest-scoring poses of pyrimidine-5-amine (R65) or 4-hydroxypyridazine (R76) bound to the $NADP^+$ binding site. The inclusion of pyrimidine-5-amine (R65) permitted glyoxal bisulfite to dock to the active-site with a slightly improved docking score of −7.9 kcal/mol, showing that the two compounds can bind to GapN simultaneously. Likewise, the presence of 4-hydroxypyridazine (R76) permitted glyoxal bisulfite to dock with a docking score of −7.8 kcal/mol. To

by the respective interacting residues (C-atoms in light blue). Please note that S284 in (A) adopts two alternate conformations. (E–H) Schematic diagram of the interactions between GapN and fragments R16 (E), from left to right R40_1, R40_2, R40_3 (F), R65 (G), and R76 (H). Legend: pink circle without frame color: polar amino acid; pink circle with red frame: acidic amino acid; pink circle with blue frame: basic amino acid; green circle: hydrophobic amino acid; blue arrow: backbone acceptor/donor; green arrow: sidechain acceptor/donor; red dashes: solvent contact.

Table 3. List of chemical fragments reported in this study and average *in silico* docking score over multiple poses forming identical interactions.

No.	Compound	SMILES-string (neglecting stereochemistry)	Glide SP score highest/average [kcal/mol]	On-site docking grid position	Off-site poses (% of total poses)
16	2-Cyanoacetamide	O = C(N)CC#N	−4.4/-3.9 ± 0.4	Active site	0
40	Imidazoline-2,4-dione	O = C1NC(C = N1) = O	−6.1/-5.0 ± 0.7	Active site	0
65	Pyrimidine-5-amine	NC1 = CN = CN = C1	−4.8/-4.5 ± 0.2	NAD^+-binding site	40
76	4-Hydroxypyridazine	OC1 = CC = NN = C1	−4.7/-3.3 ± 1.2	NAD^+-binding site	44

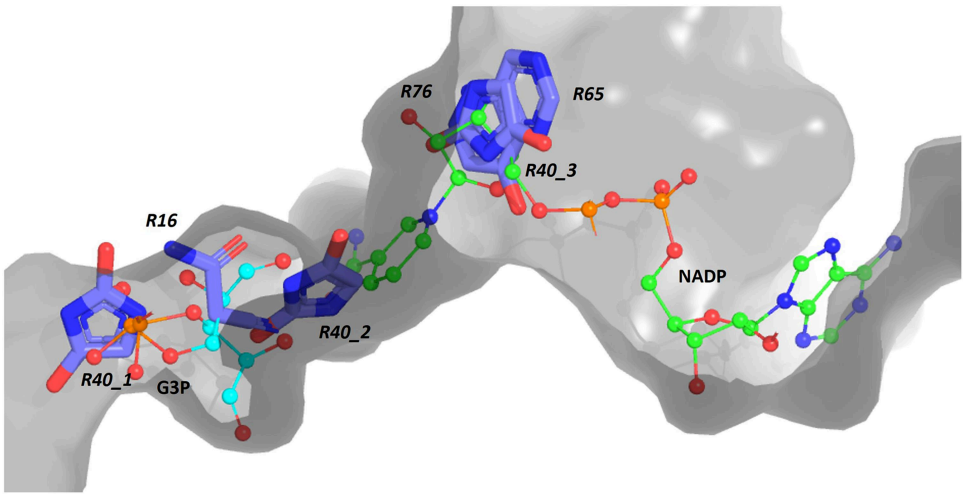

Figure 6. GapN structure with compounds targeting either the substrate or cofactor binding sites. Surface representation of GapN (chain F) in gray zoomed into the active site cleft with the fragments in stick representation (light blue C-atoms) as well as the substrate G3P with its two alternate conformations (cyan C-atoms) and the $NADP^+$ cofactor (green C-atoms) in ball-and-stick representation. The non-C-atoms are colored as follows, oxygen in red, nitrogen in blue, and phosphorous in orange.

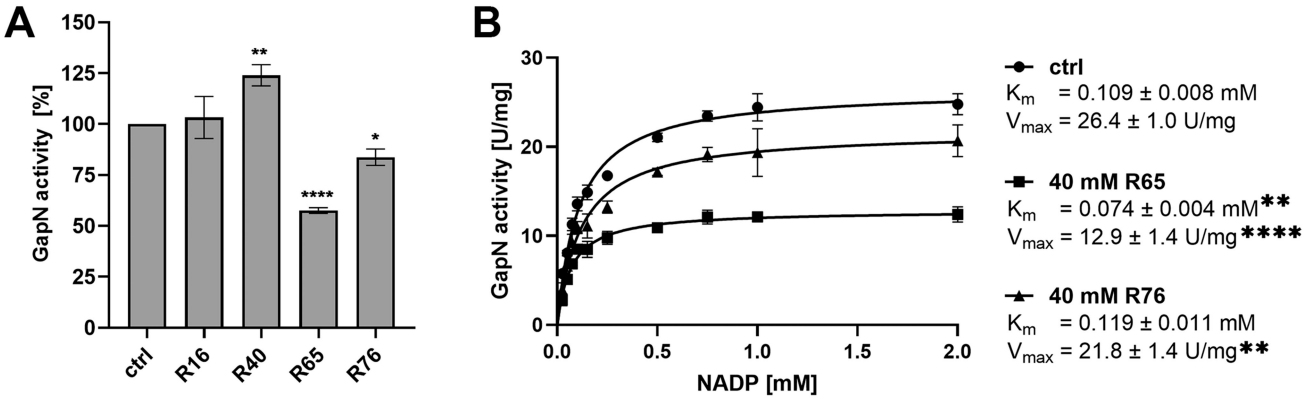

Figure 7. Influence of R65 and R76 on SpyGapN activity. (A) Effect of 40 mM of the respective fragment on the SpyGapN activity. Specific activities measured are shown relative to the specific activity of the control (1 mM DMSO) without inhibiting compound. Compound identifiers correspond to those given in Table 1. (B) Michaelis–Menten kinetics for NADP of SpyGapN in the absence and in the presence of R65 or R76 at a concentration of 40 mM. Mean values and standard deviations of $n = 3$ biological replicates. *$p <$ 0.05, **$p < 0.01$, ***$p < 0.001$, ****$p < 0.0001$ vs. control (one-way ANOVA followed by Dunnett's multiple comparisons test).

assess why only 4-hydroxypyridazine (R76) displays a synergistic effect in the presence of glyoxal bisulfite, we redocked both ultra-low-molecular-weight compounds to glyoxal bisulfite-bound GapN finding that, in its presence, both adopt multiple energetically similar docking poses that interact with the active-site residues C284 and N154 differently, likely leading to coordinated reorientations of the side chains and inhibitors within the binding-site that

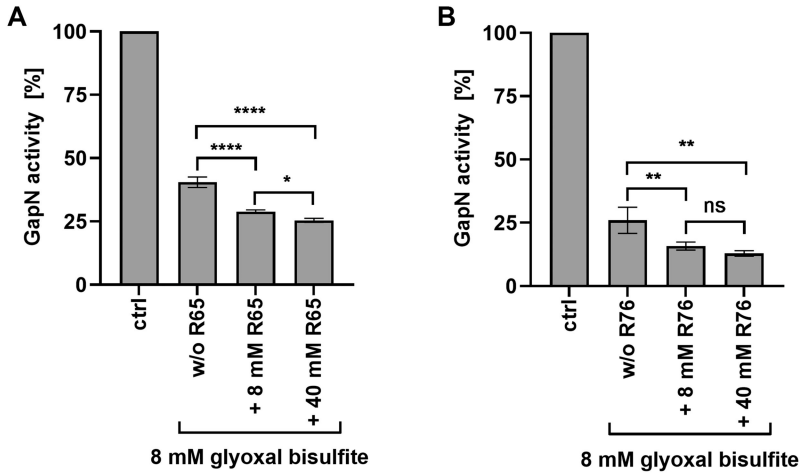

Figure 8. Influence of glyoxal bisulfite in combination with compounds R65 (A) or R76 (B) on SpyGapN enzyme activity. Fragment numbers correspond to those given in Table 1. Specific activities measured at the indicated fragment or inhibitor concentration are shown relative to the specific activity of the control (1 mM DMSO) without inhibiting compound. Mean values and standard deviations of $n = 3$ biological replicates. *$p < 0.05$, **$p < 0.01$, ***$p < 0.001$, ****$p < 0.0001$ (one-way ANOVA followed by Dunnett's multiple comparisons test).

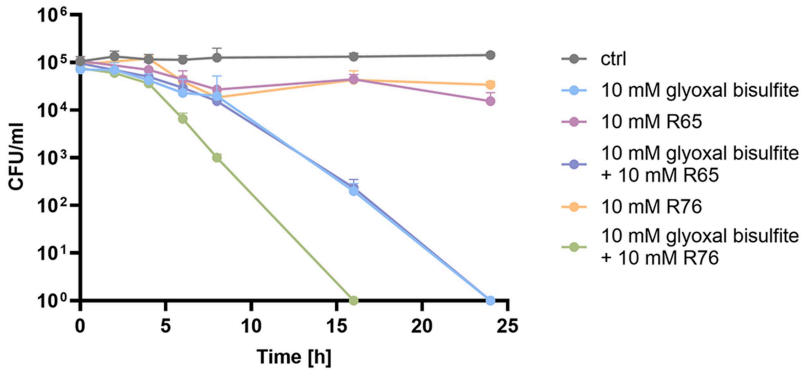

Figure 9. Killing kinetics of *S. pyogenes* M49 strain 591 for glyoxal bisulfite and fragments R65 and R76 alone or in combination. All samples were diluted to an initial bacterial concentration of 10^5 CFU/ml in BHI/Tricine buffer allowing survival but no growth, and viability was monitored over 24 h at 37°C. As control, bacteria were incubated with 1 mM DMSO. Mean values and standard deviations of $n \geq 3$ biological replicates. Statistical analysis shown in Supplementary table S2.

affect binding and catalytic activity. The corresponding docking poses are displayed in Supplementary Figure S6.

Finally, bactericidal effects of glyoxal bisulfite alone or in combination with pyrimidine-5-amine (R65) or 4-hydroxypyridazine (R76) toward *S. pyogenes* were investigated in time-kill assays (Figure 9). E4P was not included in this assay, as it can be metabolized by *S. pyogenes*. For this purpose, 10^5 CFU/ml of the bacteria were incubated with 10 mM and 20 mM of glyoxal bisulfite for 24 h, and the viable counts were determined in 2 h intervals between 0–8 h, at 16 h and at 24 h. At each time point, an untreated control was monitored for comparison. At both concentrations tested, glyoxal bisulfite completely eradicated *S. pyogenes* within 24 h (Supplementary Figure S7). The combination of 10 mM glyoxal bisulfite with 10 mM 4-hydroxypyridazine (R76) additionally accelerated the killing of the bacteria, while the combination with 10 mM pyrimidine-5-amine (R65) did not increase the killing efficiency of glyoxal bisulfite (Figure 9).

Discussion

The *in silico* screening for SpyGapN inhibitors competing with G3P was initially conducted with a homology model based on the *S. mutans* GapN structure [31,36,57]. The 32 compounds that were selected from this screening showed better docking scores than the natural substrate G3P in both the original homology model and the subsequently derived X-ray crystal structure. Docking of the 32 compounds agrees well between the homology model and the X-ray crystal structure. The slight differences in the docking scores appear to be a consequence of many small differences between the two structures and cannot be traced back solely to the different conformations of NADPH or R283.

Out of the 25 soluble candidates that were tested *in vitro*, only two compounds—glyoxal bisulfite and (ethoxyoxydophosphanyl)formate—had a significant inhibitory effect on SpyGapN activity. This indicates that docking scores showed little to no correlation to inhibition. This is not surprising given the relatively small number of compounds that have been screened, which were selected from the virtually screened compounds not primarily according to docking score but according to commercial availability. Furthermore, docking procedures generally provide more reliable poses (having been validated for predicting structures) than predictions of binding affinity, particularly for compounds binding with low affinity. More in-depth computational screening, e.g. by molecular dynamics-based methods, would vastly increase the computational load, without a guarantee of yielding improved results. They would thus only be applicable to screening smaller compound libraries, whereas our screening campaign mostly focused on commercial availability and chemical diversity under the constraints of a relatively narrow binding site and a chemically simple substrate. Thus, we emphasized coverage of chemical space over accuracy by using docking rather than slower computational methods.

Only glyoxal bisulfite reduced the SpyGapN activity by more than 50%. Glyoxal bisulfite is structurally similar to succinic acid. The charged oxygen molecules of the hydroxyl and sulfo groups of glyoxal bisulfite mediate the binding in the oxyanion hole in the G3P binding pocket formed by C284 and N154 and interact with R103, R283, and R437 that form the basic entrance region of the binding pocket.

Glyoxal bisulfite was able to efficiently eradicate *S. pyogenes* in time-kill assays. We previously showed that antisense inhibition of SpyGapN is killing *S. pyogenes* and other species lacking the oxidative part of the pentose phosphate pathway [31]. However, with the current lack of specificity of glyoxal bisulfite it is likely that its antibacterial effect against *S. pyogenes* is attributed to inhibition of both SpyGapN and SpyGapDH. To date, no antimicrobial effects or therapeutic applications are described for glyoxal bisulfite. However, it has been described to inhibit phosphoenolpyruvate carboxylase, an enzyme involved in carbon fixation in plants and some bacteria [58]. Looking more broadly, compounds with structural similarities to succinic acid, such as mercaptosuccinic acid and meso-tartrate, are already used in medical applications. Metal-complexes of mercaptosuccinic acid are used as antirheumatic therapeutics [59] as they confer anti-inflammatory effects [60,61] but can also induce oxidative stress by inhibiting glutathione peroxidase [62,63]. Antimicrobial effects against *Staphylococcus aureus* and *Bacillus subtilis* have been described for these complexes [64]. Meso-tartrate is approved by the European Medicines Agency as a therapeutic agent for stress incontinence [65]. In *Acinetobacter baumannii*, meso-tartrate was identified as an inhibitor of the essential UDP-N-acetylglucosamine acyltransferase [66]. It was shown to have antimicrobial effects against several other bacteria, e.g. *S. mutans* [67], *E. coli*, *Listeria monocytogenes*, *Salmonella typhimurium,* and *Campylobacter* spp. [68]. The antimicrobial effect was speculated to be caused by a decrease in the cytosolic pH upon meso-tartrate treatment [69].

Pyrimidine-5-amine (R65) and 4-hydroxypyridazine (R76), both occupying the $NADP^+$ binding pocket of SpyGapN, were able to increase the inhibitory effect of glyoxal bisulfite on SpyGapN activity and the latter accelerated its killing effect on *S. pyogenes*.

To the best of our knowledge, no antimicrobial effects have been described elsewhere for pyrimidine-5-amine or 4-hydroxypyridazine yet. However, generally pyridazine-derivatives have pharmacological relevance as they have been described, among others, as inhibitors of a pro-apoptotic protein kinase [70], as inhibitors of platelet aggregation [71] or as acetylcholinesterase inhibitors [72]. Aminopyrimidine derivatives include diaminopyrimidines such as Trimetoprim, a well-established dihydrofolate reductase inhibitor used as an antibacterial drug [73].

Given the low molecular weights and their classification as fragments, pyrimidine-5-amine and 4-hydroxypyridazine can be considered building blocks for the development of compounds with specific SpyGapN inhibition, as both appear to block the NADP-binding pocket. Docking of the compounds identified in the fragment screen to the crystal structure of SpyGapN was in good agreement with the measured crystallographic poses. This further validates the *in silico* approach and proves that computational design of inhibitor candidates based on the fragments is possible. Furthermore, *in silico* analysis showed that glyoxal bisulfite and pyrimidine-5-amine or 4-hydroxypyridazine can dock simultaneously and could be connected to improve additive or synergistic effects by generating a compound that occupies both the substrate and the cofactor binding site. The approach of covalently connecting different fragments within a protein binding-site, e.g. by click-chemistry, has already been demonstrated to work [74]. This could also increase the specificity of the resulting compound for SpyGapN. Another approach to solving the specificity problem could be chemical modifications of glyoxal bisulfite that allow the compound to additionally bind to

a cavity in the vestibule region of the SpyGapN substrate-binding site that is not present in SpyGapDH.

Although glyoxal bisulfite caused the strongest inhibition of SpyGapN among the compounds tested here, it was still a less effective *in vitro* inhibitor of SpyGapN than the known GapN inhibitor E4P, which was used as a control. However, as an intermediate product of the non-oxidative part of the pentose phosphate pathway, E4P can be metabolized by *S. pyogenes* [75,76]. Nevertheless, E4P is another promising candidate due to its strong inhibitory effect and its higher specificity for SpyGapN compared to glyoxal bisulfite. Modifications would be required for E4P to prevent conversion by transaldolase or transketolase while maintaining high affinity for the G3P binding site of SpyGapN.

Previous efforts to develop new ways to combat *S. pyogenes* infections have primarily focused on vaccine development [11–18] or interference with virulence pathways or more general major metabolic pathways [19–30]. In this context, our study broadens the spectrum of possible intervention strategies by focusing on GapN, an enzyme dispensable or absent in most bacteria but central for NADPH generation in *S. pyogenes*. By exploring GapN inhibition and identifying candidate inhibitors through structure-based approaches, we introduce a complementary route for limiting *S. pyogenes* viability and pathogenic capacity, expanding the repertoire of potential metabolic targets for future therapeutic development.

Acknowledgements

We acknowledge support of the staff at beamlines P13 operated by EMBL at the DESY synchrotron in Hamburg, at beamline ID30B at the ESRF-EBS in Grenoble and MX14.1 at BESSY in Berlin. JT and RCW thank Dr. Ariane Nunes-Alves for advice during the initial stages of the computational work. Furthermore, TF and IS kindly thank Prof. André Schulz, Department of Ophthalmology, Rostock University Medical Center, for technical support.

Conception and design of the work: BK, HS, RCW, TF; generation, analysis, and interpretation of the data: IS, PE, JT, AMW, RW, BHH, HLF, EM, SB, NB, HS; Drafting of the paper: IS, JT, HS, RW, TF; revising the paper critically for intellectual content: PE, BK, AMW, BHH, HLF, EM, SB, NB, RCW. All authors approve of the version to be published and all authors agree to be accountable for all aspects of the work.

Author contributions

CRediT: **Isabell Schütt:** Formal analysis, Funding acquisition, Investigation, Methodology, Writing – original draft; **Philip Einwohlt:** Formal analysis, Investigation, Writing – review & editing; **Anna-Maria Wandinger:** Investigation, Writing – review & editing; **Jonathan Teuffel:** Investigation, Writing – original draft; **Regina Wirsing:** Investigation, Writing – original draft; **Ben H. Hlawatschke:** Investigation, Writing – review & editing; **Hanna L. Fehlauer:** Formal analysis, Investigation, Writing – review & editing; **Sebastian Bothe:** Investigation, Writing – review & editing; **Nicole Bader:** Investigation, Writing – review & editing; **Emanuele Monaci:** Investigation, Writing – review & editing; **Bernd Kreikemeyer:** Conceptualization, Writing – review & editing; **Hermann Schindelin:** Conceptualization, Formal analysis, Investigation, Writing – original draft; **Rebecca C. Wade:** Conceptualization, Writing – review & editing; **Tomas Fiedler:** Conceptualization, Formal analysis, Visualization, Writing – original draft.

Funding

RCW and JT gratefully acknowledge the Klaus Tschira Foundation for financial support. IS was supported by a scholarship of the University of Rostock. PE was supported by a scholarship of the Landesgraduiertenfoerderung Mecklenburg-Vorpommern.

Disclosure statement

No potential conflict of interest was reported by the author(s).

Data availability statement

All GapN crystal structures were deposited in the Protein Data Bank (https://www.rcsb.org/) and are accessible via the following identifiers: (1) Ternary GapN-NADP$^+$-G3P complex: PDB entry 9RAZ; (2) fragment-bound structures: GapN-R16 PDB entry 9RB1, GapN-R40 9RAS, GapN-R65 PDB entry 9RAU and GapN-R76 PDB entry 9RAV.

The raw data supporting the findings of this study have been deposited in the Zenodo repository and include experimental datasets (biological replicate data underlying figures and tables) and computational modeling data. The data can be accessed via https://doi.org/10.5281/zenodo.15773859 [77].

ORCID

Isabell Schütt http://orcid.org/0009-0002-3996-7166
Bernd Kreikemeyer http://orcid.org/0000-0001-9527-5098
Tomas Fiedler http://orcid.org/0000-0001-6717-1865

References

[1] Carapetis JR, Steer AC, Mulholland EK. The global burden of group A streptococcal diseases. The Lancet Infect Dis. 2005;5(11):685–694. doi: 10.1016/S1473-3099(05)70267-X

[2] Roth GA, Mensah GA, Johnson CO, et al. Global burden of cardiovascular diseases and risk factors, 1990–2019. J Am Coll Cardiol. 2020;76(25):2982–3021. doi: 10.1016/j.jacc.2020.11.010

[3] Rwebembera J, Beaton AZ, de Loizaga SR, et al. The global impact of rheumatic heart disease. Curr Cardiol Rep. 2021;23(11):160. doi: 10.1007/s11886-021-01592-2
[4] Musser JM, Beres SB, Zhu L, et al. Reduced in vitro susceptibility of Streptococcus pyogenes to β-lactam antibiotics associated with mutations in the pbp2x gene is geographically widespread. J Clin Microbiol. 2020;58(4). doi: 10.1128/JCM.01993-19
[5] Southon SB, Beres SB, Kachroo P, et al. Population genomic molecular epidemiological study of macrolide-resistant Streptococcus pyogenes in Iceland, 1995 to 2016: identification of a large clonal population with a pbp2x mutation conferring reduced in vitro β-lactam susceptibility. J Clin Microbiol. 2020;58(9). doi: 10.1128/JCM.00638-20
[6] Vannice KS, Ricaldi J, Nanduri S, et al. Streptococcus pyogenes pbp2x mutation confers reduced susceptibility to β-lactam antibiotics. Clin Infect Dis. 2020;71(1):201–204. doi: 10.1093/cid/ciz1000
[7] Ikeda T, Suzuki R, Jin W, et al. Isolation of group A streptococci with reduced in vitro β-lactam susceptibility harboring amino acid substitutions in penicillin-binding proteins in Japan. Antimicrob Agents Chemother. 2021;65(12):e0148221. doi: 10.1128/AAC.01482-21
[8] Powell LM, Choi SJ, Chipman CE, et al. Emergence of erythromycin-resistant invasive group A Streptococcus, West Virginia, USA, 2020–2021. Emerg Infect Dis. 2023;29(5):898–908. doi: 10.3201/eid2905.221421
[9] Centers for Disease Control and Prevention (U.S.). Antibiotic resistance threats in the United States, 2019. Atlanta (GA): CDC; 2019.
[10] World Health Organization. Who bacterial priority pathogens list 2024: bacterial pathogens of public health importance, to guide research, development, and strategies to prevent and control antimicrobial resistance. 1st ed. Geneva: World Health Organization; 2024.
[11] Brouwer S, Rivera-Hernandez T, Curren BF, et al. Pathogenesis, epidemiology and control of group A Streptococcus infection. Nat Rev Microbiol. 2023;21(7):431–447. doi: 10.1038/s41579-023-00865-7
[12] Wang J, Ma C, Li M, et al. Streptococcus pyogenes: pathogenesis and the current status of vaccines. Vaccines (Basel). 2023;11(9):1510. doi: 10.3390/vaccines11091510
[13] Dale JB, Penfound TA, Chiang EY, et al. New 30-valent M protein-based vaccine evokes cross-opsonic antibodies against non-vaccine serotypes of group A streptococci. Vaccine. 2011;29(46):8175–8178. doi: 10.1016/j.vaccine.2011.09.005
[14] Dale JB, Penfound TA, Tamboura B, et al. Potential coverage of a multivalent M protein-based group A streptococcal vaccine. Vaccine. 2013;31(12):1576–1581. doi: 10.1016/j.vaccine.2013.01.019
[15] Harbison-Price N, Sebina I, Bolton RA, et al. An mRNA vaccine encoding five conserved group A Streptococcus antigens. Nat Commun. 2025;16(1):5439. doi: 10.1038/s41467-025-60580-0
[16] Widomski C, Bruyns C, Schiavolin L, et al. Beyond the emm-type: fine-tuning group A Streptococcus typing with enn and mrp. Microbiol Spectr. 2025:e0204725. doi: 10.1128/spectrum.02047-25
[17] Mora M, Bensi G, Capo S, et al. Group A Streptococcus produce pilus-like structures containing protective antigens and Lancefield T antigens. Proc Natl Acad Sci U S A. 2005;102:15641–15646. doi: 10.1073/pnas.0507808102
[18] Chochua S, Metcalf BJ, Li Z, et al. Population and whole genome sequence based characterization of invasive group A streptococci recovered in the United States during 2015. MBio. 2017;8(5). doi: 10.1128/mBio.01422-17
[19] Zhou H, Yuan Z, Guan X-N, et al. Structure-based development of a covalent inhibitor targeting Streptococcus pyogenes over Staphylococcus aureus sortase A. Chem A Eur J. 2025;31(23):e202500464. doi: 10.1002/chem.202500464
[20] Yamawaki T, Nakakido M, Nagatoishi S, et al. Development of a small compound that regulates the function of a maltodextrin-binding protein of Streptococcus pyogenes by multifaceted screenings. Sci Rep. 2025;15(1):19341. doi: 10.1038/s41598-025-02175-9
[21] Cho KH. Molecular targets in Streptococcus pyogenes for the development of anti-virulence agents. Genes (Basel). 2024;15(9):1166. doi: 10.3390/genes15091166
[22] Trivedi K, LaRock CN. Pentamidine inhibition of streptopain attenuates Streptococcus pyogenes virulence. Microbiol Spectr. 2025;13(8):e0075825. doi: 10.1128/spectrum.00758-25
[23] Molasky NMR, Zhang Z, Gillespie JR, et al. A novel methionyl-tRNA synthetase inhibitor targeting Gram-positive bacterial pathogens. Antimicrob Agents Chemother. 2024;68(12):e0074524. doi: 10.1128/aac.00745-24
[24] Kuo C-F, Chen Y-Y, Chiu C-C, et al. Comparative in vitro efficacy of AR-12 derivatives against Streptococcus pyogenes. J Antimicrob Chemother. 2025;80(3):717–725. doi: 10.1093/jac/dkae462
[25] Barkowsky G, Lemster A-L, Pappesch R, et al. Influence of different cell-penetrating peptides on the antimicrobial efficiency of PNAs in Streptococcus pyogenes. Mol Ther Nucleic Acids. 2019;18:444–454. doi: 10.1016/j.omtn.2019.09.010
[26] Abt C, Gerlach LM, Bull J, et al. Pyrenebutyrate enhances the antibacterial effect of peptide-coupled antisense peptide nucleic acids in Streptococcus pyogenes. Microorganisms. 2023;11(9):2131. doi: 10.3390/microorganisms11092131
[27] Zou W, Sun R, Yao A, et al. A promising antibiotic candidate, brevinin-1 analogue 5R, against drug-resistant bacteria, with insights into its membrane-targeting mechanism. Comput Struct Biotechnol J. 2023;21:5719–5737. doi: 10.1016/j.csbj.2023.11.031
[28] Chandole PK, Pawar TJ, Olivares-Romero JL, et al. Exploration of novel cationic amino acid-enriched short peptides: design, SPPS, biological evaluation and in silico study. RSC Adv. 2024;14(25):17710–17723. doi: 10.1039/d3ra08313f
[29] Tivari SR, Kokate SV, Delgado-Alvarado E, et al. A novel series of dipeptide derivatives containing indole-3-carboxylic acid conjugates as potential antimicrobial agents: the design, solid phase peptide

synthesis, in vitro biological evaluation, and molecular docking study. RSC Adv. 2023;13(35):24250–24263. doi: 10.1039/d3ra04100j

[30] Zou Z, Singh P, Pinkner JS, et al. Dihydrothiazolo ring-fused 2-pyridone antimicrobial compounds treat Streptococcus pyogenes skin and soft tissue infection. Sci Adv. 2024;10(31):eadn7979. doi: 10.1126/sciadv.adn7979

[31] Eisenberg P, Albert L, Teuffel J, et al. The non-phosphorylating glyceraldehyde-3-phosphate dehydrogenase GapN is a potential new drug target in Streptococcus pyogenes. Front Microbiol. 2022;13:802427. doi: 10.3389/fmicb.2022.802427

[32] Levering J, Fiedler T, Sieg A, et al. Genome-scale reconstruction of the Streptococcus pyogenes M49 metabolic network reveals growth requirements and indicates potential drug targets. J Biotechnol. 2016;232:25–37. doi: 10.1016/j.jbiotec.2016.01.035

[33] Le Breton Y, Belew AT, Valdes KM, et al. Essential genes in the core genome of the human pathogen Streptococcus pyogenes. Sci Rep. 2015;5(1):9838. doi: 10.1038/srep09838

[34] Patenge N, Rückert C, Bull J, et al. Whole-genome sequence of Streptococcus pyogenes strain 591, belonging to the genotype emm49. Microbiol Resour Announc. 2021;10(43):e0081621. doi: 10.1128/MRA.00816-21

[35] Waterhouse A, Bertoni M, Bienert S, et al. Swiss-model: homology modelling of protein structures and complexes. Nucleic Acids Res. 2018;46(W1):W296–W303. doi: 10.1093/nar/gky427

[36] Cobessi D, Tête-Favier F, Marchal S, et al. Structural and biochemical investigations of the catalytic mechanism of an NADP-dependent aldehyde dehydrogenase from Streptococcus mutans. J Mol Biol. 2000;300(1):141–152. doi: 10.1006/jmbi.2000.3824

[37] DeLano WL. Unraveling hot spots in binding interfaces: progress and challenges. Curr Opin Struct Biol. 2002;12(1):14–20. doi: 10.1016/s0959-440x(02)00283-x

[38] Friesner RA, Banks JL, Murphy RB, et al. Glide: a new approach for rapid, accurate docking and scoring. 1. Method and assessment of docking accuracy. J Med Chem. 2004;47(7):1739–1749. doi: 10.1021/jm0306430

[39] Sastry GM, Adzhigirey M, Day T, et al. Protein and ligand preparation: parameters, protocols, and influence on virtual screening enrichments. J Comput Aided Mol Des. 2013;27(3):221–234. doi: 10.1007/s10822-013-9644-8

[40] Schimunek J, Seidl P, Elez K, et al. A community effort in SARS-CoV-2 drug discovery. Mol Inf. 2024;43(1):e202300262. doi: 10.1002/minf.202300262

[41] Holderbach S, Adam L, Jayaram B, et al. Raspd+: fast protein-ligand binding free energy prediction using simplified physicochemical features. Front Mol Biosci. 2020;7:601065. doi: 10.3389/fmolb.2020.601065

[42] R Core Team. R: a language and environment for statistical computing [Computer software]; 2021.

[43] Moret M, Friedrich L, Grisoni F, et al. Generative molecular design in low data regimes. Nat Mach Intell. 2020;2(3):171–180. doi: 10.1038/s42256-020-0160-y

[44] Arya R, Prashar V, Kumar M. Evaluating stability and activity of SARS-CoV-2 PLpro for high-throughput screening of inhibitors. Mol Biotechnol. 2022;64(1):1–8. doi: 10.1007/s12033-021-00383-y

[45] Iddar A, Valverde F, Serrano A, et al. Purification of recombinant non-phosphorylating NADP-dependent glyceraldehyde-3-phosphate dehydrogenase from Streptococcus pyogenes expressed in E. coli. Mol Cell Biochem. 2003;247(1–2):195–203. doi: 10.1023/A:1024112027440

[46] Kabsch W. Acta crystallographica. Sect D Biol Crystallogr. 2010;66(2):125–132. doi: 10.1107/S0907444909047337

[47] Tickle IJ, Flensburg C, Keller P, et al. Staraniso anisotropy & Bayesian estimation server. 2016 [cited 2025 Nov 7]. Available from: https://staraniso.globalphasing.org/cgi-bin/staraniso.cgi

[48] Agirre J, Atanasova M, Bagdonas H, et al. The CCP4 suite: integrative software for macromolecular crystallography. Acta Crystallogr D Struct Biol. 2023;79(6):449–461. doi: 10.1107/S2059798323003595

[49] Murshudov GN, Skubák P, Lebedev AA, et al. Refmac5 for the refinement of macromolecular crystal structures. Acta Crystallogr D Biol Crystallogr. 2011;67(4):355–367. doi: 10.1107/S0907444911001314

[50] Emsley P, Lohkamp B, Scott WG, et al. Features and development of Coot. Acta Crystallographica. Acta Crystallogr D Biol Crystallogr. 2010;66(4):486–501. doi: 10.1107/S0907444910007493

[51] Liebschner D, Afonine PV, Baker ML, et al. Macromolecular structure determination using X-rays, neutrons and electrons: recent developments in Phenix. Acta Crystallogr D Struct Biol. 2019;75(10):861–877. doi: 10.1107/S2059798319011471

[52] Chen VB, Arendall WB, Headd JJ, et al. MolProbity: all-atom structure validation for macromolecular crystallography. Acta Crystallogr D Biol Crystallogr. 2010;66(1):12–21. doi: 10.1107/S0907444909042073

[53] Crow VL, Wittenberger CL. Separation and properties of NAD+- and NADP+-dependent glyceraldehyde-3-phosphate dehydrogenases from Streptococcus mutans. J Biol Chem. 1979;254(4):1134–1142. doi: 10.1016/S0021-9258(17)34179-0

[54] O'Reilly M, Cleasby A, Davies TG, et al. Crystallographic screening using ultra-low-molecular-weight ligands to guide drug design. Drug Discov Today. 2019;24(5):1081–1086. doi: 10.1016/j.drudis.2019.03.009

[55] Duarte D, Vale N. Evaluation of synergism in drug combinations and reference models for future orientations in oncology. Curr Res Pharmacol Drug Discov. 2022;3:100110. doi: 10.1016/j.crphar.2022.100110

[56] Bliss CI. The toxicity of poisons applied jointly. Ann Appl Biol. 1939;26(3):585–615. doi: 10.1111/J.1744-7348.1939.TB06990.X

[57] Cobessi D, Tête-Favier F, Marchal S, et al. Apo and holo crystal structures of an NADP-dependent aldehyde dehydrogenase from Streptococcus mutans 1 1edited by R. Huber. J Mol Biol. 1999;290(1):161–173. doi: 10.1006/jmbi.1999.2853

[58] Mukerji SK, Yang SF. Phosphoenolpyruvate carboxylase from spinach leaf tissue: inhibition by sulfite ion. Plant Physiol. 1974;53(6):829–834. doi: 10.1104/pp.53.6.829

[59] Brandt U, Deters A, Steinbüchel A. A jack-of-all-trades: 2-mercaptosuccinic acid. Appl Microbiol Biotechnol. 2015;99(11):4545–4557. doi: 10.1007/s00253-015-6605-2

[60] Hopkins SJ, Jayson MIV, van der Zeil P. Inhibition of lymphocyte activation by gold sodium thiomalate. Br J Pharmacol. 1983;79(2):617–622. doi: 10.1111/j.1476-5381.1983.tb11037.x

[61] Newman PM, To SS, Robinson BG, et al. Effect of gold sodium thiomalate and its thiomalate component on the in vitro expression of endothelial cell adhesion molecules. J Clin Invest. 1994;94(5):1864–1871. doi: 10.1172/JCI117536

[62] Chaudiere J, Wilhelmsen EC, Tappel AL. Mechanism of selenium-glutathione peroxidase and its inhibition by mercaptocarboxylic acids and other mercaptans. J Biol Chem. 1984;259(2):1043–1050. doi: 10.1016/S0021-9258(17)43563-0

[63] Behnisch-Cornwell S, Laubenstein G, Bednarski PJ. Studies of the inhibitory activities of tiopronin and mercaptosuccinic acid on glutathione peroxidase and their cytotoxic and antioxidant properties. Pharmazie. 2019;74(9):536–542. doi: 10.1691/ph.2019.9472

[64] Gizer SG, Şahiner N. The effect of sulphur on the antibacterial properties of succinic acid-Cu(II) and mercaptosuccinic acid-Cu(II) MOFs. Inorganica (rome) Acta. 2021;528:0020–1693. doi: 10.1016/j.ica.2021.120611

[65] European Medicines Agency. European Medicines Agency decision of 31 March 2010 on the granting of a product specific waiver for tartaric acid (EMEA-000772-PIP01-09). In: Accordance with regulation (EC) No 1901/2006 of the European Parliament and of the Council. 2010. cited 2025 Nov 7]. Available from: https://www.ema.europa.eu/en/documents/pip-decision/p-41-2010-european-medicines-agency-decision-31-march-2010-granting-product-specific-waiver-tartaric-acid-emea-000772-pip01-09-accordance-regulation-ec-no-1901-2006-european-parliam_en.pdf

[66] Badie OH, Basyony AF, Samir R. Computer-based identification of potential druggable targets in multidrug-resistant Acinetobacter baumannii: a combined in silico. Vitro In Vivo Study Microorganisms 2022. 2022;10(10):1973. doi: 10.3390/microorganisms10101973

[67] Jeong J-H, Kim S-H, Huh C-K. Separation and identification of an antimicrobial substance from Schisandra chinensis extract against Streptococcus mutans KCCM 40105 strain. Molecules. 2023;28(8):3417. doi: 10.3390/molecules28083417

[68] Over KF, Hettiarachchy N, Johnson MG, et al. Effect of organic acids and plant extracts on Escherichia coli O157: h7, Listeria monocytogenes, and Salmonella typhimurium in broth culture model and chicken meat systems. J Food Sci. 2009;74(9):M515–21. doi: 10.1111/j.1750-3841.2009.01375.x

[69] Ricke SC. Perspectives on the use of organic acids and short chain fatty acids as antimicrobials. Poult Sci. 2003;82(4):632–639. doi: 10.1093/ps/82.4.632

[70] Velentza AV, Wainwright MS, Zasadzki M, et al. An aminopyridazine-based inhibitor of a pro-apoptotic protein kinase attenuates hypoxia-ischemia induced acute brain injury. Bioorg Med Chem Lett. 2003;13(20):3465–3470. doi: 10.1016/s0960-894x(03)00733-9

[71] Coelho A, Sotelo E, Fraiz N, et al. Pyridazines. Part 36: synthesis and antiplatelet activity of 5-substituted-6-phenyl-3(2H)-pyridazinones. Bioorg Med Chem Lett. 2004;14(2):321–324. doi: 10.1016/j.bmcl.2003.11.009

[72] Contreras JM, Parrot I, Sippl W, et al. Design, synthesis, and structure–activity relationships of a series of 3-[2-(1-benzylpiperidin-4-yl)ethylamino]pyridazine derivatives as acetylcholinesterase inhibitors. J Med Chem. 2001;44(17):2707–2718. doi: 10.1021/jm001088u

[73] Hawser S, Lociuro S, Islam K. Dihydrofolate reductase inhibitors as antibacterial agents. Biochem Pharmacol. 2006;71(7):941–948. doi: 10.1016/j.bcp.2005.10.052

[74] Mondal M, Unver MY, Pal A, et al. Fragment-based drug design facilitated by protein-templated click chemistry: fragment linking and optimization of inhibitors of the aspartic protease endothiapepsin. Chem A Eur J. 2016;22(42):14826–14830. doi: 10.1002/chem.201603001

[75] Williams JF, Blackmore PF, Duke CC, et al. Fact, uncertainty and speculation concerning the biochemistry of D-erythrose-4-phosphate and its metabolic roles. Int J Biochem. 1980;12(3):339–344. doi: 10.1016/0020-711X(80)90112-3

[76] Stincone A, Prigione A, Cramer T, et al. The return of metabolism: biochemistry and physiology of the pentose phosphate pathway. Biol Rev. 2015;90(3):927–963. doi: 10.1111/brv.12140

[77] Schütt I, Fiedler T, Teuffel J, et al. Datasets accompanying the manuscript "Inhibitors of GapN-dependent NADPH supply may qualify as potential lead compounds for novel therapeutics against Streptococcus pyogenes". 2025. doi:10.5281/zenodo.15773859